THE ASTROPHYSICAL JOURNAL, 554:173–189, 2001 June 10

NEW CLASS II METHANOL MASERS IN W3(OH)

E. C. SUTTON,[1] A. M. SOBOLEV,[2] S. P. ELLINGSEN,[3] D. M. CRAGG,[4] D. M. MEHRINGER,[1]
A. B. OSTROVSKII,[2] AND P. D. GODFREY[4]
Received 2000 August 22; accepted 2001 January 30

ABSTRACT

We report interferometric observations of nine class II methanol maser candidate lines toward W3(OH). Narrow maser emission spikes at $v_{\rm LSR} = -43.1$ km s^{-1} are present in three of the lines: 3_1–4_0 A^+, 7_2–6_3 A^+, and 7_2–6_3 A^-. For all three lines the maser position is near the northern edge of the W3(OH) ultracompact H II region (maser emission is also seen near the southern edge in the 3_1–4_0 A^+ line). For the remaining six lines there is no obvious counterpart to the narrow maser spike at -43.1 km s^{-1}. Additional spatially extended emission is present in all nine lines over the range from -41 to -48 km s^{-1}. By comparing our observed flux densities with an extensive set of model calculations, we infer physical characteristics of the maser region. In these calculations the methanol is excited by infrared radiation from warm dust, and this excited gas amplifies the free-free background emission from the ultracompact H II region. The gas forming the narrow maser spikes appears to have both high kinetic temperature, $T_{\rm kin} \geq 110$ K, and high density, $n_{\rm H_2} \approx 10^7$ cm^{-3}. Low-temperature solutions are ruled out by the observed line ratios and low-density solutions by the unphysically large path length that would be required. The gas is rich in methanol ($2N_M = N_A + N_E \gtrsim 10^{-6} N_{\rm H_2}$), and the methanol column density in the tangential direction for each symmetry species (divided by line width) is $N_M/\Delta V \approx 10^{12}$ cm^{-3} s. Somewhat lower values of $n_{\rm H_2}$ and $N_M/\Delta V$ are also acceptable. The size of the region emitting the maser spike is of order 100 × 1000 AU. In most of the lines the broad emission from -41 to -48 km s^{-1} can also be attributed to weak maser action, produced in gas with similar physical conditions (high density and temperature). It differs from the narrow spike emission mainly through a beaming factor that can be interpreted as an elongation factor for clumps of maser gas. The combination of narrow and broad emission can arise naturally from an ensemble of clumps of different elongations and orientations. In this unified picture the best fit to the data is provided by $n_{\rm H_2} \approx 2 \times 10^6$ cm^{-3} and $N_M/\Delta V \approx 4 \times 10^{11}$ cm^{-3} s, somewhat lower than the values obtained for just the spike component. The methanol maser clumps may be present in an expanding shell surrounding the H II region, similar to the material producing OH maser emission in this source.

Subject headings: H II regions — ISM: clouds — ISM: individual (W3) — ISM: molecules — masers — radio lines: ISM

1. INTRODUCTION

Interstellar methanol masers were first seen by Barrett, Schwartz, & Waters (1971) in the Orion Nebula, although it took several years before their status as masers was established. To date, approximately 30 masing transitions of methanol have been detected, some with flux densities greater than 5000 Jy and brightness temperatures in excess of 10^{12} K. Methanol masers are divided into two classes. The class I methanol masers, which include those first seen by Barrett et al., are seen in massive star forming regions, but these masers are typically well separated from strong embedded infrared sources, ultracompact H II regions, and OH masers. Class II methanol masers, on the other hand, are found in the immediate vicinity of young stellar objects, usually near OH masers and ultracompact H II regions. This method of classifying methanol maser sources was developed by Batrla et al. (1987) and Menten (1991a). Sobolev (1993) has proposed further subdivisions of these two main classes.

The mechanism for the class I masers is thought to be collisional pumping, followed by a radiative cascade that preferentially overpopulates the $K = 0$ ladder in the A symmetry species and $K = -1$ in the E species (Menten 1991a). The class II mechanism, on the other hand, is less well understood. The pump seems to involve radiative excitation, and the earliest suggestions were that this took the form of radiative excitation of torsionally excited states by infrared radiation (Wilson et al. 1985; Menten et al. 1985). The class II methanol masers are subject to strong infrared radiation from warm dust that has been heated by the nearby young stellar object. Menten (1991a) suggested that radiative excitation to the first torsionally excited state ($v_t = 1$) may be sufficient to explain the class II masers in the A symmetry species, although the E-species class II masers were more problematic. Subsequent calculations by Cragg et al. (1992) were able to reproduce in a qualitative fashion the behavior of all of the class II masers using only a submillimeter radiation field and excitation within the ground ($v_t = 0$) torsional state. However, the calculated maser brightnesses in their model were smaller than the values actually observed. Subsequent work by Sobolev & Deguchi (1994a) and Sobolev, Cragg, & Godfrey (1997a, 1997b), using a mechanism involving pumping through both first

[1] University of Illinois, 1002 West Green Street, Urbana, IL 61801; sutton@astro.uiuc.edu, dmehring@astro.uiuc.edu.
[2] Astronomical Observatory, Ural State University, Lenin Street 51, Ekaterinburg 620083, Russia; andrej.sobolev@usu.ru, osan@mail.ur.ru.
[3] School of Mathematics and Physics, University of Tasmania, GPO Box 252-21, Hobart, Tasmania 7001, Australia; simon.ellingsen@utas.edu.au.
[4] Department of Chemistry, Monash University, Clayton, Victoria 3800, Australia; dinah.m.cragg@sci.monash.edu.au, peter.godfrey@sci.monash.edu.au.

and second torsionally excited states ($v_t = 1, 2$), was able to reproduce the observed brightnesses of the strong 6.7 and 12.2 GHz masers.

All models of methanol masers indicate the need for large methanol abundances, $N(CH_3OH) \gtrsim 10^{-6} N(H_2)$. Such methanol abundances are not plausible for gas phase chemical reactions and are thought to be the result of grain mantle evaporation. Caselli, Hasegawa, & Herbst (1993) have shown that enhanced methanol abundances are expected in collapsing protostellar cores due to thermal evaporation of grain mantles. In the vicinity of massive young stellar objects, evaporation is likely due to shocks associated with outflows or ionization fronts (Dreher & Welch 1981; Bachiller et al. 1995; Hartquist et al. 1995).

W3(OH) is considered the prototypical class II methanol maser source. Almost all known class II maser lines have been seen in W3(OH), and it is among the brightest known sources in the strong 5_1–6_0 A^+ (6.7 GHz) and 2_0–3_{-1} E (12.2 GHz) lines. W3(OH) contains an expanding ultracompact H II (UCH II) region surrounding a young O7 star at a distance of about 2.2 kpc (Humphreys 1978; Dreher & Welch 1981; Wilson, Johnston, & Mauersberger 1991; Kawamura & Masson 1998). To its east is W3(H_2O), a region containing water vapor masers and a young stellar object known as the TW object (Turner & Welch 1984). Molecular material is widely distributed throughout the W3(OH)/W3(H_2O) complex (Wink et al. 1994; Wyrowski et al. 1999; A. M. Sobolev, E. C. Sutton, & I. I. Zinchenko 2001, in preparation). In W3(OH) itself, the embedded UCH II region is located near clouds of warm dense gas that give rise to strong OH masers. There is considerable evidence that the material producing both the OH and methanol maser emission is located in front of the western half of the UCH II region. This evidence includes the opacity of the ionized gas at low frequencies and the detection of absorption lines against the free-free continuum, in particular methanol 10_1–9_2 A^- absorption (Wilson et al. 1991) and OH absorption (Guilloteau, Baudry, & Walmsley 1985; Baudry et al. 1993).

In order to better understand the class II maser mechanism and the physical characteristics of the masing material in W3(OH), we have searched for additional masing transitions in this source using the list of candidate lines in Sobolev et al. (1997b). We report class II maser emission in three of those transitions. One of these, 3_1–4_0 A^+, was previously seen by Val'tts et al. (1995) and Slysh et al. (1999b), although our data provide additional information. The 7_2–6_3 $A^\pm$ lines have been reported as weak class II masers in G345.01+1.79 but not previously in W3(OH) (Sobolev et al. 1999; Cragg et al. 2001). We also report significant upper limits to the flux density of maser emission in several additional lines. These measurements and upper limits provide useful constraints on the class II maser pump mechanism, as well as on physical conditions in the source.

2. OBSERVATIONS

We carried out observations of W3(OH) with the BIMA[5] 10-element interferometer in A, B, and C configurations between 1997 October and 1999 November. The phase calibrator was 0102+584 before 1998 November 1 and 0359+509 after that date. Flux density calibration was based on observations of Mars, checked by occasional observations of Jupiter and Saturn. We believe our flux density scale to be accurate to within about ±10%.

Spectral resolution was determined by the setup of the digital correlator. For most of the data reported here, the correlator channel spacing was 48.8 kHz, corresponding to velocity channel spacings between 0.13 and 0.18 km s^{-1} depending on the line frequencies. Some data were obtained with channel spacings of 24.4 and 390 kHz. No smoothing was applied, so the spectral response was a sinc function, and the effective resolution was 1.21 times the channel spacing. The flexibility of the correlator allowed us to observe some pairs of lines with only a single local oscillator setting. In one set of observations the 7_2–6_3 $A^\pm$ lines were observed simultaneously in the same sideband. And in two cases, lines were observed simultaneously in opposite sidebands: 3_1–4_0 A^+ with 7_2–8_1 A^+ and 7_2–8_1 A^- with 13_{-3}–14_{-2} E.

Accurate rest frequencies are essential for interpretation of velocity structure. We consider the calculated frequencies in Xu & Lovas (1997) to be the most useful general tabulation available for methanol. They have the additional advantage of being internally self-consistent. In some cases measured frequencies are available. We have used the measured values in a few cases, particularly when they have significantly smaller uncertainties. Our adopted rest frequencies are presented in Table 1.

We reduced the data in conventional fashion using the MIRIAD software package for editing, calibrating, and constructing spectral data cubes. The majority of the data were taken in B array, which determined the spatial resolution of the resulting maps. With robust weighting and robustness parameters in the range 0–0.6, we obtained spatial resolutions of order 1.″5–2.″5. In a few cases with high

TABLE 1

REST FREQUENCIES

Transition	Frequency (MHz)	Reference
5_1–6_0 A^+	6668.5192 ± 0.0008	1
2_0–3_{-1} E	12178.597 ± 0.004	1
2_1–3_0 E	19967.427 ± 0.007	2
9_2–10_1 A^+	23121.024 ± 0.03	3
4_0–3_1 E	28316.031 ± 0.008	2
8_2–9_1 A^-	28969.954 ± 0.020	2
7_{-2}–8_{-1} E	37703.696 ± 0.013	2
6_2–5_3 A^-	38293.292 ± 0.014	2
6_2–5_3 A^+	38452.653 ± 0.014	2
7_2–8_1 A^-	80993.257 ± 0.019	2
13_{-3}–14_{-2} E.....	84423.706 ± 0.021	2
6_{-2}–7_{-1} E	85568.074 ± 0.013	2
7_2–6_3 A^-	86615.602 ± 0.014	2
7_2–6_3 A^+	86902.947 ± 0.014	2
8_3–9_2 E	94541.806 ± 0.019	2
3_1–4_0 A^+	107013.812 ± 0.01	3
0_0–1_{-1} E	108893.929 ± 0.015	2
7_2–8_1 A^+	111289.601 ± 0.019	2
8_0–8_{-1} E	156488.858 ± 0.013	2
2_1–3_0 A^+	156602.346 ± 0.013	2
7_0–7_{-1} E	156828.480 ± 0.013	2
5_0–5_{-1} E	157178.962 ± 0.013	2
4_0–4_{-1} E	157246.041 ± 0.014	2

REFERENCES.—(1) Breckenridge & Kukolich 1995. (2) Xu & Lovas 1997. (3) Tsunekawa et al. 1995.

[5] The Berkeley-Illinois-Maryland Association operates the BIMA array under support from the National Science Foundation.

signal-to-noise ratios, the restoring beam was chosen to be 10%–20% smaller than the synthesized beam, giving a small degree of superresolution. The phase center of the maps is α(J2000) = $2^h27^m03^s.87$, δ(J2000) = 61°52′24″.6, close to the center of the ultracompact H II region in W3(OH). This phase center is 0″.6 south and 0″.3 east of the reference position of Menten et al. (1992) and Moscadelli et al. (1999), which was the position of the strongest 6.7 and 12.2 GHz masers. Our phase center is 0″.2 north of the nominal reference position of Menten et al. (1988a, 1988b). Comparison of different data sets indicates a positional accuracy of order 0″.1. The data were self-calibrated using both the line and continuum fluxes. The continuum was then subtracted from the UV data set prior to constructing the spectral data cubes.

3. RESULTS

We have measured three transitions that exhibit a "spike + pedestal" line shape, as shown in Figures 1*a*–1*c*. Parameters describing the spike and pedestal components are listed in Tables 2 and 3, respectively. The spike component in these three lines is strong and narrow and undoubtedly represents maser emission. The nature of the pedestal emission is less clear and will be discussed in § 4.5 below. In six other lines, we see only the pedestal component, as shown in Figures 1*d*–1*i*. The characteristics of the emission in these nine transitions are discussed in the sections that follow. Interpretation of the results follows in § 4.

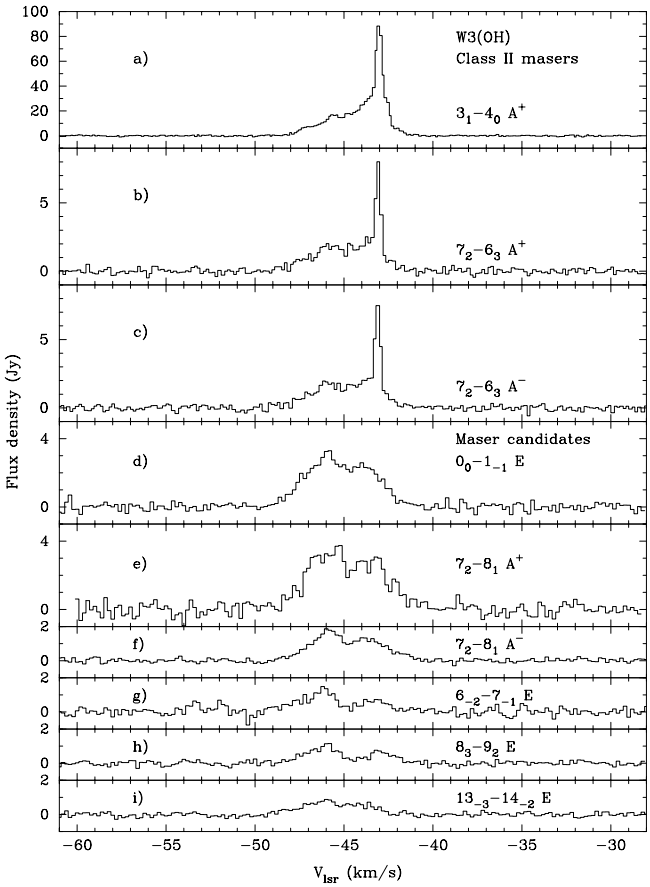

FIG. 1.—Spectra of methanol lines in W3(OH). (*a*–*c*) Three methanol lines showing class II maser emission and a spike + pedestal line shape. (*d*–*i*) Six additional maser candidate lines showing only the pedestal component. The flux density is that contained in a 4″ × 4″ box around our nominal map center of α(J2000) = $2^h27^m03^s.87$, δ(J2000) = 61°52′24″.6. The size of the box was chosen to show both the spike and pedestal components clearly.

3.1. 3_1–4_0 A^+

We see strongest emission in the 3_1–4_0 A^+ transition at 107.0 GHz. Channel maps of this line are shown in Figure 2, and a spectrum of the region in Figure 1*a*. The peak channel at $v_{LSR} = -43.1$ km s^{-1} contains a bright unresolved component plus spatially extended emission. The unresolved component is located 0″.6 north and 0″.2 west of our map center, near the northern limb-brightened edge of the UCH II region (Dreher & Welch 1981; Guilloteau, Stier, & Downes 1983; Wilson et al. 1991; Baudry & Menten 1995) where OH 7762 and 8136 MHz absorption at this velocity also peaks (Baudry et al. 1993). This position is also coincident with the reference position of the strongest 6.7 and 12.2 GHz masers (Menten et al. 1992; Moscadelli et al. 1999), within the positional uncertainty of 0″.1. A second unresolved component is clearly seen in the −42.7 km s^{-1} channel at a position 1″.2 south and 0″.5 west of map center, somewhat south of the southern edge of the UCH II region. The remaining emission from −48.0 to −41.8 km s^{-1} is concentrated in a 1″ × 2″ region that is elongated north-south, centered about 0″.5 west of map center and coincident with the western half of the UCH II region.

Peak flux densities in the northern and southern components are 72 and 22 Jy, respectively. The corresponding integrated fluxes are 30 and 15 Jy km s^{-1}. Since the two compact components are at similar velocities, both contribute to the spike feature seen in Figure 1*a*. The total integrated flux in the map is 126 Jy km s^{-1}, leaving 81 Jy km s^{-1} for the pedestal feature in Figure 1*a*. Figure 2 shows that the pedestal emission is spatially extended.

Menten et al. (1992) present measurements of methanol 6.7 GHz maser emission in W3(OH) and define a number of clusters of maser spots. The counterpart of our northern component is the cluster they label $\mathcal{M}6$. Moscadelli et al. (1999) report 41 distinct 12.2 GHz maser spots in this region. Our southern component corresponds to the 6.7 GHz cluster $\mathcal{M}1$, with possible contributions from $\mathcal{M}2$, $\mathcal{M}3$, $\mathcal{M}4$, and $\mathcal{M}5$. Moscadelli et al. report six 12.2 GHz spots in the $\mathcal{M}5$ region but none near $\mathcal{M}1$, $\mathcal{M}2$, $\mathcal{M}3$, or $\mathcal{M}4$. Both the northern and southern regions contain OH masers.

Emission in this line in W3(OH) was first seen in a single-dish spectrum taken with the Onsala 20 m telescope by Val'tts et al. (1995). They saw a spectral shape similar to that shown in Figure 1*a* and for the spike component report a v_{LSR} of -43.3 ± 0.6 km s^{-1}, based on an assumed rest frequency of 107,013.67 MHz. After transforming to the rest frequency adopted in Table 1, this becomes a v_{LSR} of -42.9 ± 0.6 km s^{-1}, consistent with our result within the rather large uncertainty. With a velocity resolution of 0.7 km s^{-1}, they report a width of 0.8 ± 0.1 km s^{-1}. After deconvolution of their spectral resolution, this result is also consistent with our observed line width. They reported integrated fluxes of 23.4 and 46.8 Jy km s^{-1} for spike and pedestal components, respectively, in rough agreement with our results.

Slysh et al. (1999b) report high-resolution interferometric observations of this line in W3(OH). Their maps clearly show a double-lobed distribution with the peaks separated north-south by about 1″.8, similar to our result. The peak

TABLE 2

CHARACTERISTICS OF THE SPIKE COMPONENT

Transition	v_{LSR}[a] (km s^{-1})	Δv (km s^{-1})	S (Jy)	$\int S\,dv$ (Jy km s^{-1})	Reference
3_1–4_0 A^+	-43.08 ± 0.05[b]	0.39 ± 0.04[b]	72 ± 7[b]	30 ± 3[b]	1
	-42.76 ± 0.10[c]	0.64 ± 0.17[c]	22 ± 1[c]	15 ± 4[c]	1
7_2–6_3 A^+	-43.13 ± 0.08	0.31 ± 0.05	7.2 ± 0.4	2.4 ± 0.4	1
7_2–6_3 A^-	-43.14 ± 0.06	0.33 ± 0.05	6.7 ± 0.3	2.4 ± 0.4	1
7_2–8_1 A^+	...	...	<1.0[d]	<0.5[d]	1
7_2–8_1 A^-	...	...	<0.3[d]	<0.12[d]	1
0_0–1_{-1} E	...	...	<0.6[d]	<0.24[d]	1
6_{-2}–7_{-1} E	...	...	<0.7[d]	<0.28[d]	1
8_3–9_2 E	...	...	<0.4[d]	<0.15[d]	1
13_{-3}–14_{-2} E.....	...	...	<0.3[d]	<0.13[d]	1
9_2–10_1 A^+	-43.12 ± 0.4	0.30 ± 0.01	9.5 ± 0.2	3.0 ± 0.1	2, 3[e]
8_2–9_1 A^-	-43.14 ± 0.23[f]	0.30 ± 0.01	13.8 ± 0.7	4.4 ± 0.3	4
6_2–5_3 A^+	-43.22 ± 0.11	0.34 ± 0.03	~ 9	2.8 ± 0.3	5
6_2–5_3 A^-	-43.23 ± 0.11	0.26 ± 0.02	~ 14	3.7 ± 0.3	5
4_0–4_{-1} E	-43.23 ± 0.21[g]	0.89 ± 0.56[g]	13.5 ± 6.8[g]	13 ± 1[g]	6
5_0–5_{-1} E	-43.26 ± 0.12[h]	0.91 ± 0.32[h]	24.2 ± 6.9[h]	23 ± 1[h]	6
7_0–7_{-1} E	-43.22 ± 0.08[i]	0.85 ± 0.03[i]	32.7 ± 1.6[i]	29 ± 2[i]	6
8_0–8_{-1} E	-43.27 ± 0.03[j]	1.08 ± 0.02[j]	27.9 ± 1.0[j]	32 ± 2[j]	6
4_0–3_1 E	-43	...	-0.6[k]	-0.2[k]	7
2_1–3_0 A^+	...	...	$\lesssim 9$	$\lesssim 3$	6

[a] All velocities have been transformed to be consistent with the rest frequencies listed in Table 1. Uncertainties in the rest frequencies have been added in quadrature with the reported velocity errors.

[b] Northern component, as discussed in text.

[c] Southern component, as discussed in text.

[d] Upper limits of 3 σ.

[e] Strongest component of Menten et al. 1988a ($v_{LSR} = -43.15$, $\Delta v = 0.38$ km s^{-1}) is located in the south.

[f] Frequency was not stated to sufficient precision; assumed to be value from Anderson, Herbst, & De Lucia 1992.

[g] Or $v_{LSR} = -43.23 \pm 0.05$, $\Delta v = 0.87 \pm 0.09$, $S = 13.4 \pm 1.3$, and $\int S\,dv = 12.5 \pm 1.2$ (Slysh et al 1999a).

[h] Or $v_{LSR} = -43.33 \pm 0.02$, $\Delta v = 1.95 \pm 0.00$, $S = 16.4 \pm 0.8$, and $\int S\,dv = 34.0 \pm 1.7$ (Slysh et al 1999a).

[i] Or $v_{LSR} = -43.20 \pm 0.08$, $\Delta v = 0.49 \pm 0.03$, $S = 36.1 \pm 1.7$, and $\int S\,dv = 18.8 \pm 0.9$ (Slysh et al 1999a).

[j] Or $v_{LSR} = -43.23 \pm 0.03$, $\Delta v = 0.90 \pm 0.06$, $S = 20.6 \pm 0.8$, and $\int S\,dv = 19.7 \pm 0.8$ (Slysh et al 1999a).

[k] Estimated value. The spike component is not evident in Wilson et al. 1993.

REFERENCES.—(1) This work. (2) Wilson et al. 1984. (3) Menten et al. 1985. (4) Wilson et al. 1993. (5) Haschick et al. 1989. (6) Slysh et al. 1995. (7) Slysh et al. 1992.

flux density in their main component is reported to be 83.5 Jy, and their integrated flux is 120 Jy km s^{-1}, both of which are in excellent agreement with our results. A more detailed comparison with our results is difficult due to some apparent inconsistencies in their paper (e.g., between their Fig. 2 and their Table 1). One point of possible disagreement between their results and ours concerns the absolute positioning, with their map offset from ours by about 0.″6. Our absolute positioning of both line and continuum emission is consistent with previous measurements summarized by Moscadelli et al. (1999).

Overall, our data for the 3_1–4_0 A^+ line are in good qualitative agreement with the spike+pedestal line shape of Val'tts et al. We also see the double-lobed spatial distribution of Slysh et al. and have good quantitative agreement with some aspects of their results. One important piece of new information is the absolute position of the 107.0 GHz maser, needed for comparison with maser components of other transitions. In the discussion that follows we will rely on our own results. We have good reason to trust both our flux density scale and our positions, as will be discussed further in § 3.6.

3.2. 7_2–6_3 $A^\pm$

The 86 GHz 7_2–6_3 $A^\pm$ lines are in the same transition series as the 38 GHz 6_2–5_3 $A^\pm$ maser lines. The A^+ and A^- components lie at 86.9 and 86.6 GHz, respectively, and form an asymmetry doublet. The asymmetry splitting is small for $K = 2$ and 3, so these transitions have nearly the same energies, line strengths, and radiative and collisional rates. It is not surprising that their spectra (Figs. 1*b* and 1*c* and Tables 2 and 3) and maps (Fig. 3) are so similar. The peak flux densities in the spike component, based on two-component Gaussian decompositions, are 7.2 and 6.7 Jy, respectively, for A^+ and A^-. For both lines the integrated fluxes in the spike component are 2.4 Jy km s^{-1}. The spike emission in these lines is spatially compact and coincident with the bright northern component seen in 3_1–4_0 A^+, within an uncertainty of about 0.″1. The 7_2–6_3 $A^\pm$ lines are weaker than 3_1–4_0 A^+. Their spike components have nearly the same v_{LSR} as the northern component of 3_1–4_0 A^+, although their line widths are somewhat narrower. It appears that all three lines show maser emission from the same physical material, which has a v_{LSR} of -43.1 km s^{-1}

TABLE 3

CHARACTERISTICS OF THE PEDESTAL COMPONENT

Transition	E_u (K)	$\mu^2 S$[a] (D^2)	S_{ave}[b] (Jy)	$\int S\,dv$ (Jy km s^{-1})	Reference
3_1–4_0 A^+	28.3	3.01	14.3 ± 1.4[c]	81 ± 8[c]	1
7_2–6_3 A^+	102.7	1.36	1.6 ± 0.2[c]	8.8 ± 1.0[c]	1
7_2–6_3 A^-	102.7	1.36	1.5 ± 0.2[c]	8.6 ± 1.0[c]	1
7_2–8_1 A^+	102.7	2.34	2.9 ± 0.3[c]	15.8 ± 1.6[c]	1
7_2–8_1 A^-	102.7	2.52	1.3 ± 0.1[c]	6.9 ± 0.7[c]	1
0_0–1_{-1} E	13.1	0.98	2.5 ± 0.3[c]	13.0 ± 1.3[c]	1
6_{-2}–7_{-1} E	74.7	2.01	0.7 ± 0.1[c]	4.3 ± 0.4[c]	1
8_3–9_2 E	131.3	2.24	0.6 ± 0.1[c]	3.5 ± 0.4[c]	1
13_{-3}–14_{-2} E.....	273.9	4.30	0.6 ± 0.1[c]	3.2 ± 0.3[c]	1
9_2–10_1 A^+	142.2	3.15	...	4.7 ± 0.2	2
8_2–9_1 A^-	121.3	3.02	...	2.8 ± 0.4	3
6_2–5_3 A^+	86.5	0.95	...	8.0 ± 0.7	4
6_2–5_3 A^-	86.4	0.95	...	9.1 ± 0.8	4
4_0–4_{-1} E	36.3	4.17	...	179 ± 4[d]	5
5_0–5_{-1} E	47.9	4.96	...	159 ± 2[e]	5
7_0–7_{-1} E	78.1	6.27	...	80 ± 5[f]	5
8_0–8_{-1} E	96.6	6.78	...	64 ± 3[g]	5
4_0–3_1 E	36.3	1.40	...	−1.4 ± 0.4[h]	6
2_1–3_0 A^+	21.4	2.00	...	111 ± 4	5

[a] The S in $\mu^2 S$ is line strength, not flux density.
[b] Average from −44 to −47 km s^{-1}.
[c] Uncertainties dominated by systematic errors, estimated to be of order 10%.
[d] Slysh et al. 1999a give 181 ± 4 for the same data set.
[e] Slysh et al. 1999a give 154 ± 2 for the same data set.
[f] Slysh et al. 1999a give 100 ± 5 for the same data set.
[g] Slysh et al. 1999a give 99 ± 4 for the same data set.
[h] After removing spike absorption. Wilson et al. 1993 give −1.2 ± 0.2.

REFERENCES.—(1) This work. (2) Wilson et al. 1984. (3) Wilson et al. 1993. (4) Haschick et al. 1989. (5) Slysh et al. 1995. (6) Slysh et al. 1992.

and is located in front of the northern edge of the UCH II region. The 7_2–6_3 $A^{\pm}$ lines show no evidence for the southern lobe seen in 3_1–4_0 A^+.

3.3. 7_2–8_1 $A^{\pm}$

The 7_2–8_1 $A^{\pm}$ lines fall at 111.3 and 81.0 GHz. The large difference in frequency is due to the rather large asymmetry splitting in $K = 1$. These lines belong to the same transition series as the 23.1 GHz 9_2–10_1 A^+ and 29.0 GHz 8_2–9_1 A^- masers. The upper levels of the 111.3 and 81.0 GHz lines are 7_2 $A^{\pm}$, the same upper levels as the 86 GHz lines reported in § 3.2 above. Since the 86 GHz lines show the spike emission profile that we attribute to maser emission, it would be reasonable to expect maser emission in these lines as well. This general expectation is borne out by the calculations of Sobolev et al. (1997b), although there are some physical conditions under which the 81.0 and 111.3 GHz lines are predicted to be significantly stronger than the 86 GHz lines and vice versa. Evidently, the masing region in W3(OH) fits the latter situation, since the spectral signature of the 81.0 and 111.3 GHz lines does not show a spike component (Figs. 1*e* and 1*f*). We estimate upper limits to the peak flux density in such a component to be 1.0 and 0.3 Jy for the A^+ and A^- lines, respectively, and upper limits to the integrated fluxes to be 0.5 and 0.12 Jy km s^{-1}. The implications of these limits are discussed in § 4.4 below.

3.4. 0_0–1_{-1} E

The 108.9 GHz line 0_0–1_{-1} E involves levels of low excitation energy (1_{-1} E is the ground state of E-species methanol). This transition is predicted to mase under certain physical conditions (Sobolev et al. 1997b) and has been seen masing in G345.01+1.79 (Val'tts et al. 1999). It also belongs to the same transition series as the strong 12.2 GHz 2_0–3_{-1} E maser line. Realistic scenarios for W3(OH) involve a range of physical conditions. Since the 0_0 E and 1_{-1} E levels are low energy and are significantly populated throughout the region, there may be significant quasi-thermal emission and/or absorption present at 108.9 GHz in addition to any possible maser emission, complicating interpretation of the data from this line. However, no significant spike emission is evident in the spectrum shown in Figure 1*d*, and we estimate upper limits of 0.6 Jy and 0.24 Jy km s^{-1} to its peak and integrated fluxes.

3.5. 6_{-2}–7_{-1} E, 8_3–9_2 E, and 13_{-3}–14_{-2} E

The 6_{-2}–7_{-1} E line at 85.6 GHz belongs to the series $K = -2 \rightarrow -1$, in which an adjacent member, 7_{-2}–8_{-1} E, has been claimed as a class II maser in W3(OH) by Haschick, Baan, & Menten (1989). Further discussion of 7_{-2}–8_{-1} E appears below in § 4.3. Sobolev et al. (1997b) predict that 6_{-2}–7_{-1} E can also mase under certain conditions in high-density, low-temperature regions, and it has been seen masing in G345.01+1.79 (Sobolev et al. 1999; Cragg et al. 2001). We see no evidence of a spike component in Figure 1*g* and set upper limits to the peak and integrated fluxes of such a component of 0.7 Jy and 0.28 Jy km s^{-1}.

The 8_3–9_2 E line appears at 94.5 GHz. No class II masers are known involving the $K = 3$ ladder of the E species, but

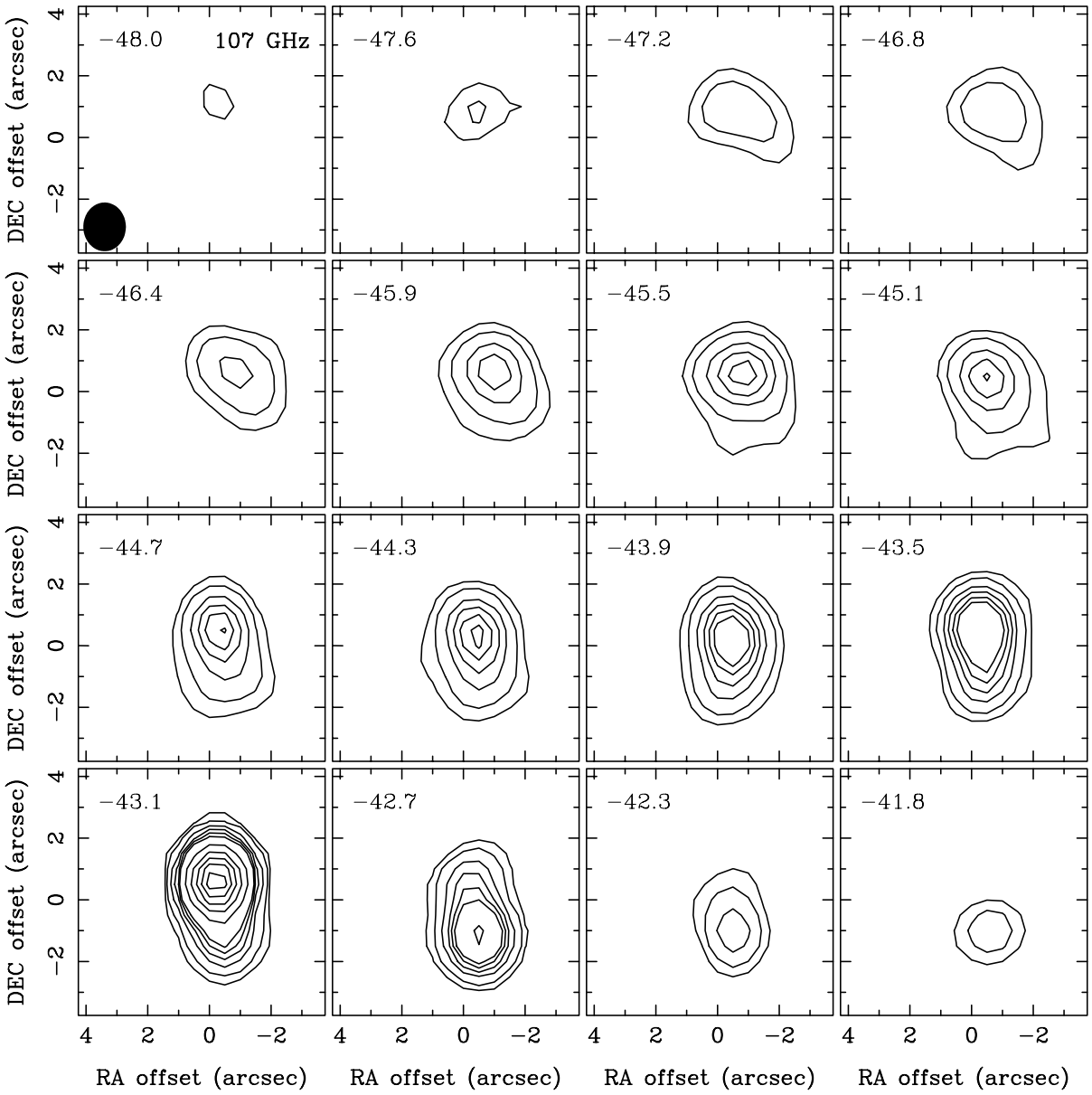

FIG. 2.—Selected channel maps of the 3_1–4_0 A^+ emission. Every third channel from −48.0 to −41.8 km s^{-1} is shown. The beam size is 1.″6 × 1.″4, and the contour levels are 1, 2, 4, 6, 8, 10, 20, 30, 40, 50, and 60 Jy beam^{-1}. The strong emission at −43.1 km s^{-1} consists of an unresolved core located 0.″6 north and 0.″2 west of the map center, plus an extended component. At redshifted velocities the emission peaks further south. Blueshifted emission is concentrated north and west of the map center.

Sobolev et al. (1997b) predict that this line can also mase at high density. We present our spectrum of this transition in Figure 1*h*. No spike component is evident, and we set upper limits of 0.4 Jy and 0.15 Jy km s^{-1}.

The 84.4 GHz line 13_{-3}–14_{-2} *E* involves levels of higher energy than the others discussed in this paper. Calculations extending the results of Sobolev et al. (1997b) predict only weak maser emission in this line. Again we see no spike component in our data, with upper limits of 0.3 Jy and 0.13 Jy km s^{-1}. Pedestal emission, however, is clearly present here and in all the transitions shown in Figure 1, the results for which are tabulated in Table 3.

3.6. *Continuum*

Although the millimeter-wave continuum of W3(OH) is not the principal topic of this investigation, we present our continuum map of this region in Figure 4, in order to confirm the positional relationship between the continuum source and the maser regions and in order to check our flux density scale. The results shown here are continuum observations obtained simultaneously with the line observations reported above. That is, they represent lower and upper sideband continua at 80.8, 83.4, 84.3, 86.9, 94.8, 98.3, 107.4, and 110.9 GHz, to which we added data at 96.6 and 99.9 GHz obtained from a parallel project. Channels corresponding to maser lines or other identified spectral features were not included. The individual sideband maps were in excellent agreement. The data were combined using the method of multifrequency synthesis. The map is presented using logarithmic contours. The emission from the UCH II region peaks 0.″2 ± 0.″1 west of our phase center and is partially resolved. The source 5.″4 east of center is the contin-

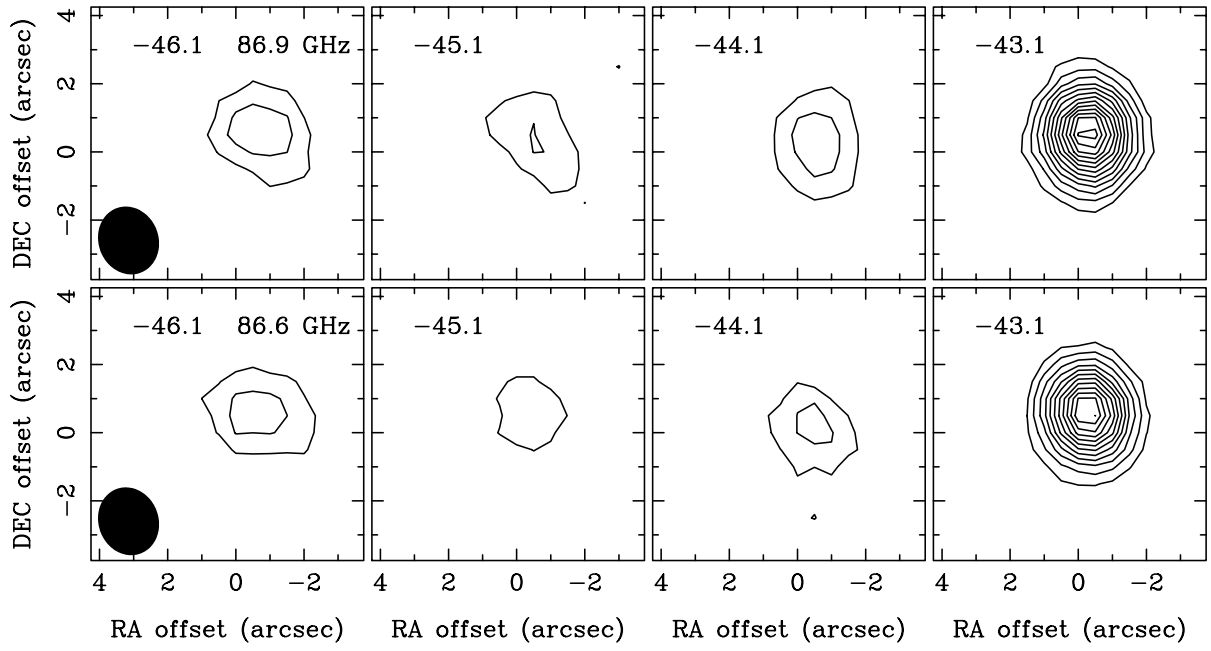

FIG. 3.—Selected channel maps of the 7_2–6_3 A^+ and 7_2–6_3 A^- emission (*top and bottom rows, respectively*). The beam size is 2.″0 × 1.″8, and the contour levels are 0.5, 1, 1.5, 2, 2.5, 3, 3.5, 4, 4.5, 5, 5.5, 6, and 6.5 Jy beam^{-1}. Plots are spaced at intervals of six channels, approximately 1 km s^{-1}. In both lines the emission peaks at −43.1 km s^{-1}, approximately 0.″6 north and 0.″3 west of the map center.

uum source associated with W3(H_2O), which is elongated east-west in agreement with previous observations (Reid et al. 1995; Wilner, Reid, & Menten 1999).

For our present purposes, there are two important results from the continuum data: (1) Our continuum position is in good agreement with the centroid of the irregularly shaped UCH II region. It is known that even at our mean frequency of 97 GHz the continuum flux density from W3(OH) itself is almost entirely free-free emission from the UCH II region [although the flux from W3(H_2O) is primarily dust emission]. (2) We measure a continuum flux density in a 4″ × 4″ box around W3(OH) to be 3.2 Jy, in good agreement with the accepted value of 3 Jy (Wilson et al. 1991; Wyrowski et al. 1999).

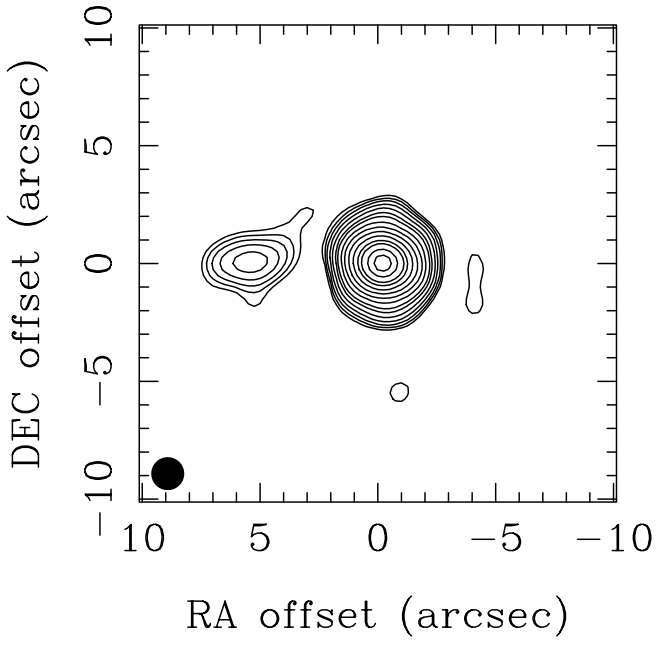

FIG. 4.—Continuum map at a mean frequency of 97 GHz, with a beam size of 1.″4 × 1.″4. Contours are 0.01, 0.015, 0.022, 0.033, 0.05, 0.075, 0.1, 0.15, 0.22, 0.33, 0.5, 0.75, 1, 1.5, and 2 Jy beam^{-1}. The emission centered about 6″ east of W3(OH) is associated with the TW object in W3(H_2O).

4. DISCUSSION

4.1. *Comparison with* 9_2–10_1 A^+, 8_2–9_1 A^-, 6_2–5_3 $A^\pm$, *and* J_0–J_{-1} E

Previously reported class II methanol maser lines in W3(OH) that exhibit the spike+pedestal profile are 9_2–10_1 A^+ (Wilson et al. 1984; Menten et al. 1985, 1988a), 8_2–9_1 A^- (Wilson et al. 1993), 6_2–5_3 $A^\pm$ (Haschick et al. 1989), and J_0–J_{-1} E, where $J = 4$, 5, 7, and 8 (Slysh, Kalenskii, & Val'tts 1995; Slysh et al. 1999a). The reported characteristics of these transitions are shown in Table 2 for ease of comparison with our results.

The velocities originally reported have been transformed to our standard velocity scale using Table 1. The uncertainties in some of the rest frequencies in Table 1 may be underestimated in that they represent formal errors in the calculated fit and do not reflect possible inadequacies in the molecular model. The velocity uncertainties shown in Table 2 are quadrature combinations of the measurement errors and the uncertainties associated with the rest frequencies. So they also are lower limits to the true uncertainties. With this in mind, the velocities for these eight lines are in good agreement with our velocities for 7_2–6_3 $A^\pm$ and the northern component of 3_1–4_0 A^+, suggesting that the spike emission in these cases arises from material with essentially the same v_{LSR}.

Most of the line widths are also similar at about 0.3 km s^{-1}. Some variation in line width is physically plausible, especially if there are several clumps of masing material with nearby velocities whose relative strengths vary from line to line.

The flux densities reported in Table 2 range over only about 1 order of magnitude and would all be described as moderate to weak maser emission. The truly strong masers in W3(OH) are orders of magnitude stronger and exhibit quite different characteristics, as will be discussed in § 4.3.

Of the lines discussed in this section, only the 23.1 GHz line 9_2–10_1 A^+ has previously been mapped interferometrically (Menten et al. 1988a). The masing region was found to be elongated north-south with a total extent of about 1".5 and the ends located near the northern and southern edges of the UCH II region. This appears similar to the spatial distributions discussed in §§ 3.1 and 3.2 for 3_1–4_0 A^+ and 7_2–6_3 $A^{\pm}$. However, the strongest spot in 9_2–10_1 A^+ was located near the *southern* edge of the UCH II region and had a $v_{\rm LSR}$ of -43.15 km s^{-1}. One of the northern spots also had a $v_{\rm LSR}$ of -43.15 km s^{-1} and therefore has the closest correspondence with our material, although that 23.1 GHz maser spot at that velocity is rather weak. It corresponds well in position with the northern component seen in Figure 2 (the map center of Menten et al. 1988a is slightly shifted with respect to our center) and with the 7_2–6_3 $A^{\pm}$ positions.

4.2. *Absorption Profiles and Upper Limits*

The transition 4_0–3_1 E was seen in absorption in W3(OH) by Slysh, Kalenskii, & Val'tts (1992) and Wilson et al. (1993). The absorption profile of Slysh et al. showed a narrow spike of about -0.6 Jy at about -43 km s^{-1} and broader, deeper (-1 Jy) absorption centered near -45 km s^{-1}. However, the spike component is not evident in the data of Wilson et al. If the results of Slysh et al. are correct, which seems likely to us given their good signal-to-noise ratio, the absorption profile of 4_0–3_1 E would be very similar to the spike + pedestal line shape that we see in emission in many of the class II maser lines.

Absorption is also seen in some lines that are class I methanol masers (Menten et al. 1986) but not in others (Liechti & Wilson 1996). The J_2–J_1 E lines reported by Menten et al. all show absorption near -45 km s^{-1}, with the higher J members of that series showing an additional absorption feature near -43 km s^{-1} (several of those lines also show *emission* near -47 km s^{-1}). Absorption over a similar range of velocities was seen in 10_1–9_2 A^- by Menten et al. (1985) and Wilson et al. (1991). Any model of the class II masers in W3(OH) should also be consistent with the absorption profiles.

Also of significance for models of this region is the nondetection of a spike component in 2_1–3_0 A^+ reported by Slysh et al. (1995). An upper limit to the integrated flux in such a component would appear to be about 3 Jy km s^{-1}. Slysh et al. (1995, 1999a) also did not detect spike components in the 6_2–7_1 $A^{\pm}$ lines, although the limits that can be set from their data only weakly constrain maser emission models.

4.3. *Other Maser Lines in W3(OH)*

The strongest maser lines in W3(OH) exhibit considerably more complex spectral profiles. The 5_1–6_0 A^+ line at 6.7 GHz and 2_0–3_{-1} E at 12.2 GHz exhibit strong emission over the range -42 to -46 km s^{-1} (Menten 1991b; Batrla et al. 1987) and appear to consist of a series of strong maser spikes. VLBI maps of these lines (Menten et al. 1992; Moscadelli et al. 1999) show the emission to come from two clusters of maser spots near the northern and southern edges of the UCH II region, similar to the distribution discussed above. However, the number and strength of the maser features in these lines, as well as model calculations (Sobolev et al. 1997b), indicate that these lines are rather easily excited under a wide range of physical conditions. Thus, much of the emission seen in these lines may come from material unrelated to that we have been discussing for the weaker lines exhibiting the spike + pedestal profile.

The 2_1–3_0 E line at 20.0 GHz (Wilson et al. 1985) appears to be a transitional case. Like the spike + pedestal lines, the strongest emission falls near -43 km s^{-1}. But the strong emission persists to the blue, a property more characteristic of the 6.7 and 12.2 GHz lines.

The observed pattern of peak flux densities is $S_{6.7} \gg S_{12.2} \gg S_{20.0}$, although there is considerable variation with velocity. For a fixed source solid angle, this implies $T_b(6.7) \gg T_b(12.2) \gg T_b(20.0)$. Looking at individual spots, Moscadelli et al. (1999) find $\log_{10}\,[T_b(6.7)/T_b(12.2)] \simeq 0$–2 for many spots, with additional lower limits to the logarithm in the same range. Considering just velocities near -43.1 km s^{-1}, this logarithmic brightness ratio is about 1.6 for a composite of the northern spots and 0.4 for the southern cluster. The brightness temperature of the 20.0 GHz line at that $v_{\rm LSR}$ is about 1 order of magnitude weaker than the 12.2 GHz line.

One other line in W3(OH) has an unusual profile, 7_{-2}–8_{-1} E at 37.7 GHz (Haschick et al. 1989). This line profile appears to be broad and redshifted, unlike any of the other maser transitions. The redshift appears to be too great to attribute to an error in the rest frequency, and model calculations indicate that this line is unlikely to mase except under high-density, low-temperature conditions. Because of the limited signal-to-noise ratio of this observation, we are unwilling to make any definite conclusions about it. Careful reobservation of this line would be useful.

4.4. *Model Calculations*

In this section we construct models of class II maser emission regions and fit those models to the observational data for W3(OH). Previous calculations of this sort were presented by Sobolev et al. (1997b). This work extends their results to a much larger region of parameter space. In these calculations we include methanol energy levels up to $J = 22$ for $v_t = 0$, 1, 2 and adopt the radiative transition rates from Mekhtiev, Godfrey, & Hougen (1999). For the W3(OH) UCH II region, we adopt an electron temperature of 10^4 K (Kawamura & Masson 1998) and a free-free turnover frequency of 12 GHz (see Dreher & Welch 1981; Baudry et al. 1993). Both parameters are known to be somewhat variable across the source; this value for the turnover frequency is likely to be near the lower end of the range actually present. These parameters imply a background brightness temperature of $10^4\{1 - \exp\,[-(1.2 \times 10^{10}/\nu)^2]\}$ K, where ν is the frequency in hertz. This background radiation is available for amplification by the methanol-rich gas in front. The remainder of the model is as described by Sobolev & Deguchi (1994a) and Sobolev et al. (1997a, 1997b). The methanol molecules are pumped to torsionally excited states by infrared radiation from warm dust, described by dust temperature T_d, filling factor 0.5, and opacity $(\nu/10^{13})^2$. Radiative transfer is treated in the large velocity gradient

(LVG) approximation, with the addition of a beaming factor ϵ^{-1}, defined as the ratio of radial to tangential optical depths, to represent the elongation of the maser region along the line of sight. Background free-free emission from the UCH II region is diluted by a geometrical factor $W_{\rm H\,II}$. Collisional transitions are treated using the model of Peng & Whiteoak (1993). The remaining parameters of the maser region are the gas kinetic temperature $T_{\rm kin}$, molecular hydrogen number density $n_{\rm H_2}$, and methanol specific column density $N_M/\Delta V$ (defined as the column density of A or E species methanol tangential to the line of sight, divided by the line width).

The new model calculations span a range of hydrogen density $n_{\rm H_2} = 10^4$–10^9 cm^{-3} and methanol specific column density $N_M/\Delta V = 10^{11}$–10^{13} cm^{-3} s, extending from the low-density radiative limit of the model to the high-density thermal limit where all masers are quenched and from the optically thin regime to the onset of saturation in the strongest maser transitions. Kinetic temperature was varied over the range $T_{\rm kin} = 30$–250 K, and the dust temperature was set to $T_d = 175$ K. The dilution factor $W_{\rm H\,II}$ was varied between 0.002, 0.02, and 0.2 and the beaming factor between $\epsilon^{-1} = 1$, 3, 10, 20, and 100. Some regions of parameter space were explored more thoroughly than others. The masers are generated by predominantly radiative processes, as shown by their prevalence at the low-density limit (Sobolev et al. 1997b). Generally speaking, the presence or absence of maser action in a line that is prone to masing depends on the parameters $n_{\rm H_2}$ and $T_{\rm kin}$, which govern the collisional quenching, while the remaining parameters govern the maser brightness temperatures. An analysis of the pumping network is given in Appendix A.

We concentrate initially on fitting the new high-resolution data presented in § 3. The spike components of the 86 GHz lines and most of the spike component at 107 GHz are presumed to originate in the same physical region, based on velocity and spatial coincidence. The six measured upper limits apply to the sum of contributions from all regions in the beam and therefore must apply to each such region individually, including that giving rise to the spike component at 86 and 107 GHz. Data from other previously measured transitions may also be considered, but there are uncertainties associated with comparing observations made at different epochs. Also, the strong maser lines at 6.7 and 12.2 GHz exhibit multiple components, often at the same $v_{\rm LSR}$, making it difficult to be certain that we are describing emission with a common origin in the same physical material.

An important parameter is the size of the maser emission region, necessary for conversion between calculated brightness temperatures and observed flux densities. Our present data give no direct measurement of size. We assume a common source size for the masers at all frequencies. This enables us to fit brightness temperature ratios, recovering the source size at the end from the absolute flux density at a single reference frequency. We define the brightness temperature ratio $R_{\rm obs} = (S_v/S_{107})(107.0/v)^2$, where S_v is the observed flux density at frequency v and S_{107} is the observed flux density at 107.0 GHz. This is compared with the ratio of model brightness temperatures, $R_{\rm calc} = T_{bv}/T_{b107}$. The assumed source size at any calculation point is obtained by equating the model brightness temperature T_{b107} with the observed flux density S_{107} in the 107.0 GHz 3_1–4_0 A^+ reference line. We use the rms of the logarithmic difference between $R_{\rm obs}$ and $R_{\rm calc}$ as a measure of the goodness of fit. Where the observed value is an upper limit, a contribution to rms is included only when $R_{\rm calc}$ exceeds the observed limit to $R_{\rm obs}$. Table 4 displays log $R_{\rm obs}$ for the maser observations, together with calculated values from illustrative models.

When the model calculations are fitted to the three lines and six upper limits reported in this paper, good fits are obtained only at temperatures above 100 K. The ratio of brightness temperature in the 81.0 GHz 7_2–8_1 A^- transition relative to that in the 86 GHz 7_2–6_3 $A^\pm$ masers is particularly sensitive to kinetic temperature. The observed upper limit to this ratio rules out low-temperature solutions. A good high-temperature, high-density fit of this sort is illustrated by model A of Table 4 ($T_{\rm kin} = 150$ K, $n_{\rm H_2} = 10^{6.8}$ cm^{-3}, $N_M/\Delta V = 10^{12.0}$ cm^{-3} s). Two of our observed lines are predicted to be in absorption: 6_{-2}–7_{-1} E at 85.6 GHz and 8_3–9_2 E at 94.5 GHz. However, the absorption is intrinsically weak, and due to the small source size, it is strongly beam diluted. No spike absorption is seen in these two lines (Figs. 1*g* and 1*h*), and according to this model, no detectable absorption is expected. Figure 5 shows the model brightness temperatures along three parameter axes for selected masers, where lines in the same transition series are grouped to show their similar excitation profiles. When the parameters are varied one at a time about model A, as in Figure 5, reasonably good fits (rms < 0.5) are obtained for kinetic temperatures $T_{\rm kin} \geq 110$ K, hydrogen densities in the range $10^{6.5}$cm$^{-3} \leq n_{\rm H_2} \leq 10^{7.0}$ cm^{-3}, and methanol specific column densities in the range $10^{11.9}$ cm^{-3} s $\leq N_M/\Delta V \leq 10^{12.2}$ cm^{-3} s. The best-fitting values of the density and specific column density parameters are correlated. Similarly good fits are obtained for somewhat higher or lower hydrogen densities if the methanol specific column density is scaled up or down in unison with the hydrogen density. This reflects a partial trade-off between quenching at higher hydrogen densities and the additional gain associated with an increase in methanol column density. Models in this region of parameter space also comply with our observed upper limits for the 108.9 GHz 0_0–1_{-1} E maser and the 13_{-3}–14_{-2} E (84.4 GHz) and 7_2–8_1 A^+ (111.3 GHz) transitions. In model A the calculated brightness temperature of the 107.0 GHz maser is 2×10^7 K, and the implied source size is about 0.″02 (40 AU at 2.2 kpc), within the range established by Slysh et al. (1999b).

The dilution factor $W_{\rm H\,II} = 0.002$ used in model A and in previous calculations (Sobolev et al. 1997b; Cragg et al. 2001) represents the case of a maser region well separated from the H II region. Our observations can also be well modeled with larger values of this parameter, as illustrated by model B in Table 4. This is again a high-temperature, high-density model with parameters close to those of model A, except that $W_{\rm H\,II} = 0.2$, representing the case where the maser region is just outside the ionized region. The predicted brightness temperatures in model B are reduced for all of the lines listed, especially the 6.7 and 12.2 GHz masers. The brightness temperature at 107.0 GHz is 10^6 K, implying the need for a larger source size ($\approx 0.1''$, equivalent to 200 AU at 2.2 kpc) in order to match the observed flux density. Except for the issue of source size, our results are largely insensitive to $W_{\rm H\,II}$.

Either of the above sizes is reasonably comparable to that of the central part of the northern clump of 6.7 GHz (Menten et al. 1992) and 12.2 GHz (Moscadelli et al. 1999)

TABLE 4

MODELS OF W3(OH) CLASS II METHANOL MASER SPIKES

TRANSITION	ν (GHz)	S_{obs} (Jy)	log R_{obs}	MODEL A[a] log R_{calc}	MODEL A[a] S_{calc} (Jy)	MODEL B[b] log R_{calc}	MODEL B[b] S_{calc} (Jy)
Current Observations, Included in the Fit							
7_2–8_1 A^-	81.0	<0.3	< -2.14	−3.22	0.0	−3.09	0.0
13_{-3}–14_{-2} E.....	84.4	<0.3	< -2.17	−4.67	0.0	−3.98	0.0
6_{-2}–7_{-1} E	85.6	<0.7	< -1.82	Abs.	0.0	Abs.	0.0
7_2–6_3 A^-	86.6	6.7	−0.85	−0.77	7.9	−0.77	7.9
7_2–6_3 A^+	86.9	7.2	−0.82	−0.85	6.7	−0.81	7.3
8_3–9_2 E	94.5	<0.4	< -2.15	Abs.	0.0	Abs.	0.0
3_1–4_0 A^+	107.0	72[c]	0	0	72.0	0	72.0
0_0–1_{-1} E	108.9	<0.6	< -2.09	−2.98	0.1	−2.17	0.5
7_2–8_1 A^+	111.3	<1.0	< -1.89	−4.39	0.0	−3.62	0.0
Previous Observations with −43.1 km s^{-1} Spike, Not Included in the Fit							
9_2–10_1 A^+	23.1	9.5	0.45	−3.20	0.0	−2.54	0.0
4_0–3_1 E	28.3	−0.6	Abs.	Abs.	0.0	Abs.	−0.1
8_2–9_1 A^-	29.0	13.8	0.42	−2.02	0.0	−1.93	0.1
6_2–5_3 A^-	38.3	14	0.18	−1.10	0.7	−0.77	1.6
6_2–5_3 A^+	38.5	9	−0.02	−1.18	0.6	−0.82	1.4
8_0–8_{-1} E	156.5	27.9	−0.74	−0.18	101.8	0.31	314.5
2_1–3_0 A^+	156.6	<9	< -1.23	−1.13	11.4	−0.64	35.3
7_0–7_{-1} E	156.8	32.7	−0.67	−0.20	97.6	0.30	308.5
5_0–5_{-1} E	157.2	24.2	−0.81	−0.20	98.1	0.31	317.3
4_0–4_{-1} E	157.2	13.5	−1.06	−0.40	61.9	0.08	186.8
Other Masers with Complex Spectra, Not Included in the Fit							
5_1–6_0 A^+	6.7	756[d]	3.43	3.02	295.6	2.29	55.0
2_0–3_{-1} E	12.2	10[e]	1.03	2.06	107.5	1.54	32.5
2_1–3_0 E	20.0	55[f]	1.34	−2.08	0.0	−1.55	0.1
7_{-2}–8_{-1} E	37.7	4.3[g]	−0.32	Abs.	0.0	Abs.	−0.1

NOTES.—The term R is the ratio of brightness temperature to that in the 107.0 GHz 3_1–4_0 A^+ transition (see text, § 4.5). All models have $T_d = 175$ K and $\epsilon^{-1} = 10$. The entry "Abs." indicates that the transition is in absorption, but all calculated absorptions are very weak (0 Jy > S_{calc} > −0.1 Jy). In addition to the lines shown here, the 23.4 GHz 10_1–9_2 A^- line and the 25 GHz J_2–J_1 E series are calculated to be in absorption, as is observed.

[a] Model A: $T_{kin} = 150$ K, $W_{HII} = 0.002$, $n_{H_2} = 10^{6.8}$ cm^{-3}, $N_M/\Delta V = 10^{12.0}$ cm^{-3}s.

[b] Model B: $T_{kin} = 150$ K, $W_{HII} = 0.2$, $n_{H_2} = 10^{7.0}$ cm^{-3}, $N_M/\Delta V = 10^{12.0}$ cm^{-3}s.

[c] Northern component only.

[d] Northern component at −43.1 km s^{-1} (Menten et al. 1992).

[e] Northern cluster at −43.1 km s^{-1} (Moscadelli et al. 1999). The flux in the southern cluster at this velocity is about 123 Jy.

[f] Wilson et al. 1985.

[g] Haschick et al. 1989.

masers. The 23.1 GHz maser regions seen by Menten et al. (1988a) were $\lesssim 0\farcs04$ in diameter. These sizes are also in good agreement with sizes of OH maser clusters (Reid et al. 1980; Baudry et al. 1988; Garcia-Barreto et al. 1988).

The previous observations of maser lines with spike components near −43.1 km s^{-1} in W3(OH) are also compared with the illustrative models in Table 4. In general, the lower frequency lines are underpredicted by our model, and the 157 GHz J_0–J_{-1} E series masers are overpredicted by factors of about 3–10. The 156.6 GHz 2_1–3_0 A^+ maser is slightly overpredicted. The 28.3 GHz line is predicted to be in absorption, as is observed. The underpredicted lines at 23.1, 29.0, 38.3, and 38.5 GHz do not present a problem for our model since the majority of the observed flux in these lines can be produced in separate regions with different physical conditions (low density and/or low temperature). Such regions would contribute little, if any, flux density to the lines reported in this paper. This is illustrated by the 23.1 GHz 9_2–10_1 A^+ line, where the strongest emission is located in the south (§ 4.1). The overpredictions do present an apparent problem, but many of the overpredictions are small and probably of the order expected, given the deficiencies of our model (discussed in Appendix B). Also, consideration of A/E abundance ratios greater than unity (Friberg et al. 1988; Menten et al. 1988c; Sobolev et al. 1997a) may help alleviate some of these overpredictions. High-resolution reobservation of some of these masers, to establish a set of observations that coincide in both position and time, would permit a better test of the model by extending the fit to a wider range of maser frequencies.

Table 4 also compares the model results with the four maser lines that show more complex spectra. The 7_{-2}–8_{-1} E (37.7 GHz) line is predicted in absorption but observed as a broad, redshifted emission feature, as dis-

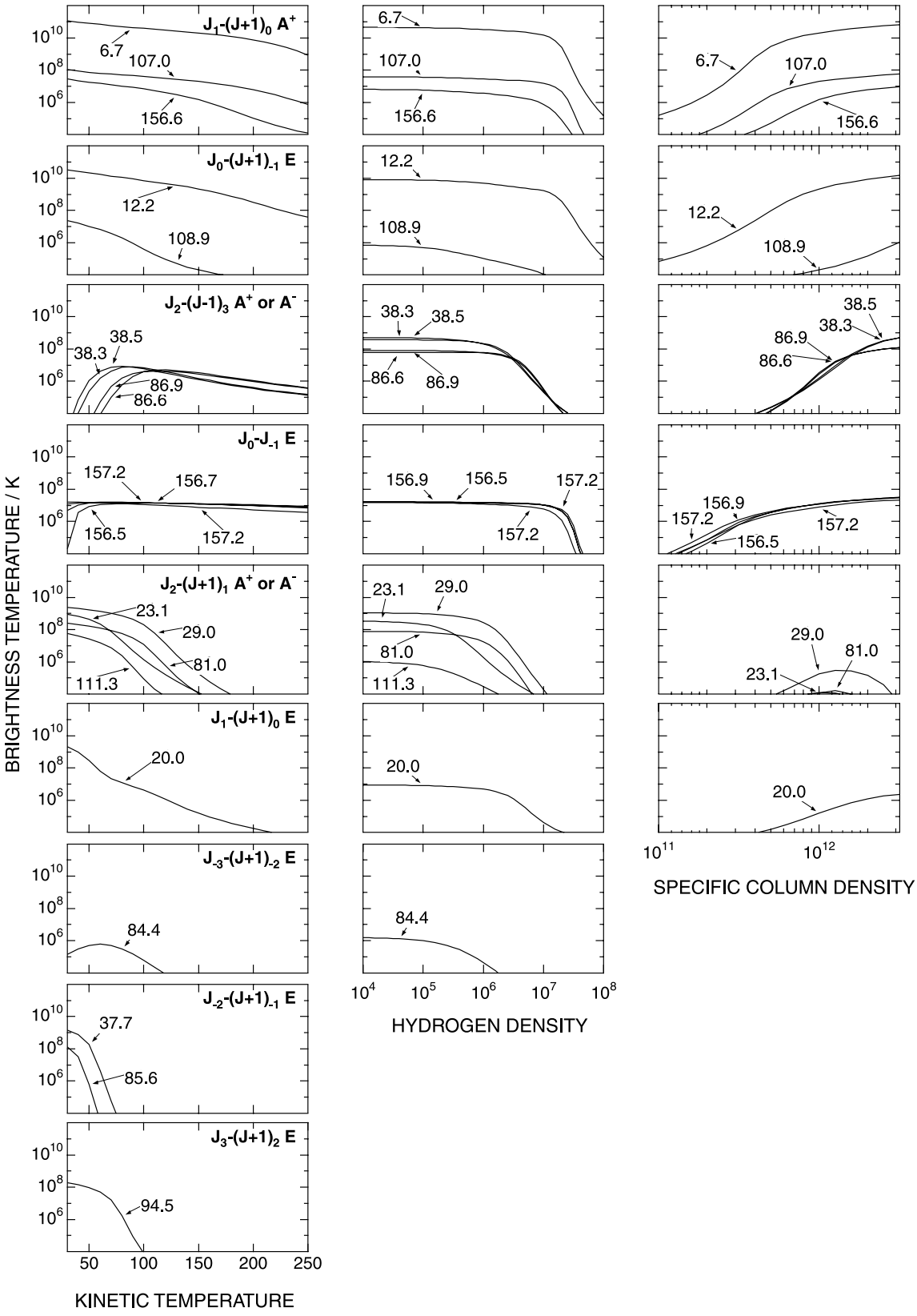

FIG. 5.—Variation of brightness temperature with model parameters for selected methanol masers. Transitions are grouped into series and labeled with the line frequency in gigahertz, but for clarity not all members of each series are shown. The plots show variation with kinetic temperature $T_{\rm kin}$ (*left panels*), hydrogen density $n_{\rm H_2}$ (*center panels*), and methanol specific column density $N_M/\Delta V$ (*right panels*). Each cut through parameter space passes through the point $T_{\rm kin} = 150$ K, $n_{\rm H_2} = 10^{6.8}$ cm^{-3}, $N_M/\Delta V = 10^{12}$ cm^{-3} s, $T_d = 175$ K, $\epsilon^{-1} = 10$, and $W_{\rm H\,II} = 2 \times 10^{-3}$. Where panels are missing, the predicted brightness temperatures of all lines in that series are less than 10^4 K over the parameter range shown.

cussed in § 4.3. The predicted absorption is too weak to have been seen in the observational data, and the emission is presumably produced in other regions of the source. The 6.7 GHz 5_1–6_0 A^+ and 20.0 GHz 2_1–3_0 E masers are generally underpredicted by the best-fitting models. The 12.2 GHz 2_0–3_{-1} E maser is overpredicted by a factor of 3–10. This raises the question of whether the strong 6.7 and 12.2 GHz masers are generated simultaneously with the weaker masers at other frequencies. The weaker maser transitions display considerably simpler spectra. Furthermore, the dominant maser components in the weaker transitions are usually less significant in the profiles of the strong transitions. The brightest components of the weaker transitions are therefore likely to arise under different conditions from those producing the brightest components of the strong transitions. Coincidence of positions and velocities of the maser spots in the weaker transitions with those at 6.7 and 12.2 GHz suggests that they arise under common conditions. But it does not require it, because the regions in which the weaker masers arise can provide seed photons for further amplification in other regions situated along the line of sight. Previous calculations (Sobolev & Deguchi 1994a; Sobolev et al. 1997a, 1997b) were mainly aimed at an explanation of the intensities of the strong maser transitions, while the new calculations described here have not been constrained by the 6.7 and 12.2 GHz VLBI data. The 20.0 and 37.7 GHz masers are brightest at low temperatures, i.e., under model conditions different from those that best fit our new observations.

Our model assumes that the pumping radiation is produced by dust external to the maser region. In reality, dust is probably intermixed with the masing gas. Since some of the pumping lines are probably optically thick in the absorbing gas, the gas in the interior of the cloud is to some extent shielded from the dust radiation. Dust internal to the cloud, if it is of significant opacity, can thus alter the pumping conditions. We have derived $\log (N_M/\Delta V) \approx 11.8$, which for $\Delta V = 0.3$ km s^{-1} implies $N_M \approx 2 \times 10^{16}$ cm^{-2}. This is the column density for each species, so assuming that the A and E species abundances are equal, the total methanol column density in the tangential direction is 4×10^{16} cm^{-2}. For a methanol fractional abundance of 10^{-6}, $N_{\rm H_2} \approx 4 \times 10^{22}$ cm^{-2}. Using the Hildebrand (1983) relation between hydrogen column density and dust opacity and a λ^{-2} dust opacity law, this implies $\tau \approx 1.4$ at 20 μm, the approximate wavelength of the bulk of the pumping photons. Although this value is uncertain, it appears that our current calculations are strictly valid only for fractional methanol abundances $\gtrsim 10^{-5}$. For lower methanol fractional abundances, the internal dust emission is significant and should be accounted for. Calculations are underway for including this internal dust and will be the subject of a future publication.

Also of interest is the length of the masing path. Here we take the column density of each symmetry species in the radial direction $\epsilon^{-1} N_M/\Delta V \approx 10^{12.8}$ cm^{-3} s, which for a fractional abundance of 10^{-5} and $n_{\rm H_2} \approx 3 \times 10^6$ cm^{-3} implies a path length of order 1.3×10^{16} cm ($\approx$1000 AU). Since the diameter of the UCH II region is of order 3000 AU, a path length of 1000 AU is plausible. However, fractional abundances of 10^{-6} or less, or physical densities of 10^5 cm^{-3} or less, begin to require uncomfortably long physical path lengths. This is a strong argument in support of our high-density model.

The constraint on the methanol fractional abundance is particularly interesting. The smallest fractional abundance consistent with the models is obtained for the case of maximum path length and physical density and minimum specific column density. Taking limiting values of $\epsilon^{-1} N_M/\Delta V = 10^{12.8}$ cm^{-3} s, $n_{\rm H_2} = 10^7$ cm^{-3}, and $L = 4 \times 10^{16}$ cm (3000 AU), we obtain a minimum fractional abundance of 10^{-6} for A and E species combined. As discussed above, our calculations begin to break down in this regime due to the influence of internal dust. Preliminary calculations indicate that internal dust is unlikely to affect the derived fractional abundance by more than about a factor of 2. So it seems likely that the fractional abundance is at least $\sim 10^{-6}$ and more likely $\sim 10^{-5}$. Values this large are likely to be due to grain mantle evaporation. In our model the gas temperature in the maser region is $\sim$150 K, indicative of conditions under which such evaporation is likely to occur (Menten et al. 1986; Caselli et al. 1993).

In comparison with the above results, multitransition methanol maser modeling has been undertaken for G345.01+1.79 and NGC 6334F by Cragg et al. (2001). The majority of observations in both sources are consistent with a warm dust ($T_d = 175$ K) pumping model at hydrogen density $\sim 10^6$ cm^{-3} and methanol column density $\sim 5 \times 10^{17}$ cm^{-2}, similar to the values obtained here for W3(OH). G345.01+1.79 is the only source in which maser action at 85.6 and 108.9 GHz has been detected to date. The 85.6 GHz 6_{-2}–7_{-1} E maser requires gas kinetic temperatures less than 90 K in the model and is quenched at the warmer gas temperatures ($T_{\rm kin} = 150$ K) derived here for W3(OH).

The 107.0 GHz 3_1–4_0 A^+ line displayed a narrow-line component in the south for which there was no 86 GHz counterpart (§§ 3.1 and 3.2). The location of this component appears to be south of the southern edge of the UCH II region, so an appropriate physical model would be one without background free-free emission. The general behavior under such circumstances is illustrated by models 8 and 9 of Sobolev et al. (1997b). All the lines observed here are weaker under such conditions, although there is an increase in the brightness temperature ratio of the 3_1–4_0 A^+ line relative to the 7_2–6_3 $A^\pm$ lines. Therefore, the presence of a 107.0 GHz maser component in the south of W3(OH) without detectable 86 GHz maser emission is quite plausible. Sobolev et al. show that under these conditions strong 6.7 GHz maser emission would still be expected but the 12.2 GHz line would be weaker. This is consistent with the general behavior of 6.7 and 12.2 GHz masers in W3(OH): the latter appear to be confined to regions with significant free-free background emission (Moscadelli et al. 1999), whereas the former can be found outside the boundary of the UCH II region (Menten et al. 1992).

4.5. *Nature of the Pedestal Emission*

All nine lines in this study show a pedestal component extending from about -48 to -41 km s^{-1}, as seen in Figure 1. The spatial distribution of this component appears to be somewhat different than that of the spike component. In the 3_1–4_0 A^+ line, the blueshifted emission is somewhat extended to the west in comparison with the map of the peak channel (Fig. 2). The blueshifted 86 GHz emission (Fig. 3) is also shifted somewhat to the west. It seems clear that there is some difference in spatial distribution between the spike and pedestal components. Five of the six

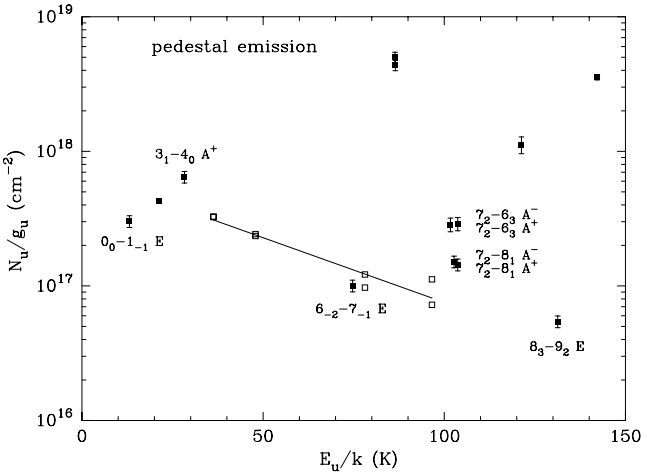

FIG. 6.—Rotation diagram of the pedestal component of emission from W3(OH). The data are taken from Table 3 and include the alternative values given in the table notes. The source size has been set to 0.″1 diameter. The labeled points are those from this paper. The point for 13_{-3}–14_{-2} E is not shown; it is off-scale to the right. Crowded points have been shifted slightly for clarity. The open boxes are for the J_0–J_{-1} series, which are well described by a thermal distribution at a temperature of 45 K, as shown.

"pedestal only" lines discussed in §§ 3.3–3.5 display similar behavior: a spatial extent of about 2″ and centered somewhat southwest of the spike position (the remaining line is 6_{-2}–7_{-1} E, which has a low signal-to-noise ratio). The fact that the blueshifted components appear to the west is consistent with maps of 7762 and 8136 MHz OH absorption, in which the absorbing gas around -45 km s^{-1} appears to overlay the entire western half of the UCH II region (Baudry et al. 1993).

The pedestal emission could represent either quasi-thermal emission or a blend of weak maser features. For the 9_2–10_1 A^+ line, Menten et al. (1985) conclude that the pedestal is produced by maser emission, based on their measured source sizes and derived brightness temperatures. Theirs is an extreme case, due to the high excitation energy of that transition. However, the pedestal components of the 6_2–5_3 $A^{\pm}$ and 8_2–9_1 A^- lines are also quite strong: assuming comparable source sizes, it would seem that they also are produced by maser emission (see Haschick et al. 1989). In Figure 6 we present a rotation diagram of the pedestal emission for the lines listed in Table 3. The pattern is distinctly nonthermal, and it seems likely that much of the pedestal emission in many of these lines may be due to maser action. Indeed, the only part of this figure with a quasi-thermal character is the behavior of the J_0–J_{-1} E series, which drops off steadily with increasing J. Pedestal emission at 85.6, 94.5, 108.9, and 156.6 GHz is also weak and possibly quasi-thermal in nature. The pedestal profiles of these lines are all very similar and roughly the same shape as the absorption profiles discussed in § 4.2. It is difficult to understand how lines of such varying energies, A coefficients, and excitation pathways should produce similar spectral profiles through maser emission, unless the amount of maser amplification is small.

If the pedestal component is attributed to weak maser emission, what are the physical characteristics of the pedestal emission region? Since the pedestal line shape is somewhat variable, we consider an average flux density from -44 to -47 km s^{-1}, as tabulated in Table 3. In non-LTE models without warm continuum radiation, we are unable to obtain an adequate fit to the observations by varying the density, kinetic temperature, and methanol column density, lending support to the idea that weak maser action is taking place. Introducing external dust radiation with $T_d = 175$ K activates the class II maser pumping and produces a good fit to the pedestal brightness temperature ratios under high-temperature, high-density conditions similar to those required for the spike (e.g., $T_{\rm kin} = 150$ K, $n_{\rm H_2} = 10^{6.8}$ cm^{-3}, and $N_M/\Delta V = 10^{12}$ cm^{-3} s). These calculations employ a beaming factor of $\epsilon^{-1} = 1$, so the effective methanol column density along the line of sight is a factor of 10 smaller than for the spike models, with a correspondingly great reduction in the maser optical depth and brightness temperature. Indeed, apart from the 107.0 GHz line, which shows significant maser amplification, the model brightness temperatures of the weak maser lines at 81.0, 84.4, 86.6, 86.9, 108.9, and 111.3 GHz are similar in magnitude to those of the 85.6 and 94.5 GHz lines, which are not inverted.

An example of a high-temperature, high-density fit to the pedestal emission is shown in Table 5, where the effects of the H II region continuum emission are also included ($T_{\rm kin} = 150$ K, $n_{\rm H_2} = 10^{6.2}$ cm^{-3}, and $N_M/\Delta V = 10^{11.6}$ cm^{-3} s). The observed brightness temperature ratios for the pedestal emission are in good agreement with the

TABLE 5

MODELS OF W3(OH) CLASS II METHANOL MASERS WITH DIFFERENT BEAMING

TRANSITION	ν (GHz)	log $R_{\rm obs}$ (PEDESTAL)	log $R_{\rm calc}$ $\epsilon^{-1} = 1$	$\epsilon^{-1} = 3$	$\epsilon^{-1} = 10$	$\epsilon^{-1} = 20$	log $R_{\rm obs}$ (SPIKE)
7_2–8_1 A^-	81.0	-0.8	-0.7	-1.1	-2.7	-2.1	<-2.1
13_{-3}–14_{-2} E.....	84.4	-1.2	-1.3	-1.8	-3.9	-4.4	<-2.2
6_{-2}–7_{-1} E	85.6	-1.1	Abs.	Abs.	Abs.	Abs.	<-1.8
7_2–6_3 A^-	86.6	-0.8	-0.6	-0.9	-2.1	-0.7	-0.9
7_2–6_3 A^+	86.9	-0.8	-0.6	-1.0	-2.1	-0.8	-0.8
8_3–9_2 E.....	94.5	-1.3	Abs.	Abs.	Abs.	Abs.	<-2.1
3_1–4_0 A^+	107.0	(>10 K)	(4×10^2 K)	(5×10^3 K)	(3×10^6 K)	(4×10^7 K)	($>5 \times 10^5$ K)
0_0–1_{-1} E	108.9	-0.8	-0.5	-1.0	-2.6	-2.4	<-2.1
7_2–8_1 A^+	111.3	-0.7	-0.9	-1.5	-3.4	-3.5	<-1.9

NOTES.—The term R is the ratio of brightness temperature to that in the 107.0 GHz 3_1–4_0 A^+ transition (see text, § 4.5). Brightness temperature of 107.0 GHz reference maser for each model is given in parentheses in units of kelvins. All models have $T_{\rm kin} = 150$ K, $T_d = 175$ K, $N_M/\Delta V = 10^{11.6}$ cm^{-3} s, $n_{\rm H_2} = 10^{6.2}$ cm^{-3}, and $W_{\rm HII} = 0.002$.

$\epsilon^{-1} = 1$ model for all lines other than 85.6 and 94.5 GHz, which display weak absorption against the H II continuum in the model calculations. As discussed above, the observed emission in those two lines may be quasi-thermal in origin. When the parameters are varied one at a time about this point, reasonably good fits (rms < 0.5, excluding the 85.6 and 94.5 GHz lines) are obtained for kinetic temperatures in the range 60 K $\leq T_{\rm kin} \leq$ 170 K, hydrogen densities $10^{4.0}$ cm^{-3} $\leq n_{\rm H_2} \leq 10^{6.4}$ cm^{-3}, and methanol specific column densities $10^{11.4}$ cm^{-3} s $\leq N_M/\Delta V \leq 10^{12.1}$ cm^{-3} s. These $\epsilon^{-1} = 1$ pedestal fits are insensitive to changes in $W_{\rm H II}$ over a wide range from 0.002 to 0.2. For the $\epsilon^{-1} = 1$ model in Table 5, the predicted brightness temperature of the 107.0 GHz reference maser is 400 K. This matches the average pedestal flux density of 14.3 Jy observed in W3(OH) (Table 3) for a source size of about 2″ diameter, a value that is sensitive to some of the model parameters. Our model is consistent with the pedestal source overlying the entire western half of the UCH II region, as suggested by the observed spatial distributions (discussed at the beginning of this section). Our calculations therefore suggest that the pedestal emission is produced in an extended region and is a complex mix of quasi-thermal and weak maser emission.

4.6. *Unified Picture*

In § 4.4 we showed that the spike emission from W3(OH) is the result of maser action in hot, dense, methanol-rich gas in front of the UCH II region, pumped by infrared radiation from warm dust. Independently, in § 4.5 we found that much of the pedestal emission is produced by weak maser action in gas of similar physical characteristics. The substantial difference between the two cases is that the maser amplification for the spike is moderate and directional, whereas that for the pedestal is weaker and directed less strongly toward the observer. This can be a result of the geometry of the maser region, which could contain some regions greatly elongated along the line of sight and others of more spherical shape (or elongated in directions other than along the line of sight). Table 5 displays examples of model calculations for the pedestal ($\epsilon^{-1} = 1$–3) and spike ($\epsilon^{-1} = 10$–20) that provide good agreement with the observed ratios, using common values of all other model parameters. This leads to the hypothesis that both the spike and pedestal emission emanate from gas with a temperature of about 150 K and a density of order 2×10^6 cm^{-3}, in the same general region around W3(OH).

The location of the spike feature at the redshifted edge of the pedestal profile provides additional information. In an expanding shell the longest paths of near-constant line-of-sight velocity occur near the limb-brightened edges. The motion of this gas is nearly in the plane of the sky, and spectral features fall near the systemic velocity. This material corresponds to the regions with high beaming factors ($\epsilon^{-1} = 10$–20) giving rise to the spike component ($v_{\rm LSR} = -43.1$ km s^{-1}), as discussed in § 4.4. The material between the observer and the center of the UCH II region appears blueshifted. The radiation from this region is *not* strongly beamed toward the observer and can be described either as clumps with low beaming factors ($\epsilon^{-1} \approx 1$) or as elongated clumps inclined from the line of sight. A superposition of such clumps gives rise to the pedestal component (§ 4.5). Material on the far side of the UCH II region does not contribute significantly since it lacks a strong background source to amplify. The general features of this scenario should hold true even with some degree of turbulence present.

This picture is consistent with other measures of the expansion. Kawamura & Masson (1998) directly measure the angular expansion of the UCH II region and derive an expansion velocity of 3–5 km s^{-1} for a distance of 2.2 kpc. The OH maser proper motion study of Bloemhof, Reid, & Moran (1992) gives transverse velocities of order 3 km s^{-1}. These are roughly consistent with our pedestal widths of about 5 km s^{-1}. Modeling their data in terms of a spherical expansion, Bloemhof et al. derive a systemic velocity in the range -44.3 to -41 km s^{-1}, strongly correlated with distance. Our data and interpretation are consistent with part of that range.

In their model Kawamura & Masson take $T = 150$ K for the dense shocked shell of gas just outside the ionized region. This temperature is the same as we find from our analysis of methanol maser excitation. Kawamura & Masson discuss densities in the range 7×10^6–7×10^7 cm^{-3} but note that this is a dynamical estimate that neglects magnetic pressure. In our calculations the 86 GHz methanol masers are predicted to be quenched at $n_{\rm H_2} \gtrsim 2 \times 10^7$ cm^{-3}. Our unified model favors densities more like 2×10^6 cm^{-3}, although models of just the spike component favor a density of about 10^7 cm^{-3}. These results are consistent with density estimates of about 10^6–10^7 cm^{-3} from OH excitation analysis (Baudry et al. 1981; Cesaroni & Walmsley 1991).

The above discussion has been framed in terms appropriate to a classical ionization-bounded nebula. A number of authors have considered more complicated scenarios for W3(OH), including champagne flows, stellar-wind bow shocks, and discrete layers of ionized gas (e.g., Guilloteau et al. 1985; van Buren et al. 1990; Wilson et al. 1991; Keto et al. 1995). Outflows from W3(H_2O) may also influence the region in front of W3(OH). The proposed champagne flow from W3(OH) extends to the north-east and is directed toward the observer (blueshifted). Our data do not contradict this model, since the methanol masers are seen in front of the *western* half of the UCH II region. They do, however, suggest that an expanding shell-like structure remains intact in the west, as also indicated by the results of Kawamura & Masson (1998). The center of the UCH II region presumably remains evacuated due to either a fast stellar wind or radiation pressure.

5. CONCLUSIONS

Class II methanol masers are pumped by infrared radiation from warm dust. Methanol-rich gas in front of the W3(OH) ultracompact H II region, excited in this fashion, amplifies the free-free continuum emission from the background H II region. From observations of nine class II methanol maser candidate lines, we reach the following conclusions:

1. The 107.0 GHz 3_1–4_0 A^+ and 86 GHz 7_2–6_3 $A^\pm$ lines exhibit narrow maser emission spikes.

2. These masers appear to originate in high-density ($n_{\rm H_2} \approx 10^7$ cm^{-3}), high-temperature ($T_{\rm kin} \geq 110$ K) material. In contrast, the masers in the 20–40 GHz range tend to favor regions of low density and/or low temperature. And although the strong 6.7 and 12.2 GHz masers can be produced under high-temperature conditions, they can also be produced at low temperature, where the 86 GHz masers are not expected.

3. This gas has high methanol abundance ($2N_M = N_A + N_E \gtrsim 10^{-6} N_{H_2}$), indicating strong methanol enrichment by grain mantle evaporation.

4. The dimensions of the region producing the spike emission are of order 100 × 1000 AU.

5. For the most part, the broad pedestal features seen in all nine lines may be attributed to maser emission arising from material with physical characteristics similar to that giving rise to the spike. The main difference is in the beaming factor ϵ^{-1}. An ensemble of clumps with different beaming factors and orientations would thus give rise to both the spike and pedestal components, as observed. In this unified picture, the optimal density ($n_{H_2} \approx 2 \times 10^6$ cm^{-3}) and column density ($N_M/\Delta V \approx 4 \times 10^{11}$ cm^{-3} s) are somewhat lower than the values derived for just the spike.

6. The observed flux density ratios are consistent with a geometrical dilution factor in the range $W_{H\,II} = 0.002$–0.2. The upper end of this range ($W_{H\,II} = 0.2$) is favored on geometrical grounds, since it corresponds to maser gas close to the H II region and is therefore consistent with the masers arising in a thin shell around the H II region.

7. The gas producing this emission seems to overlie the western half of the ultracompact H II region and is kinematically identified with gas seen in that location in OH absorption studies and OH maser emission.

8. The kinematics are consistent with an expanding thin shell.

This work was supported in part by the National Science Foundation under BIMA grants AST 96-13999 and AST 99-81363. D. M. M. acknowledges support for this work under grant AST 96-15025 to the Caltech Submillimeter Observatory. A. M. S. and A. B. O. were supported by the Russian Federal Program "Astronomy" and INTAS grant 97-11451. D. M. C. and P. D. G. acknowledge financial support from the Australian Research Council.

APPENDIX A

NETWORK ANALYSIS

We have undertaken an analysis of the pumping network in order to understand the observed strength of the 86 GHz masers and the weakness of the 81.0 GHz maser relative to the 107.0 GHz maser. These observational results rule out low-temperature models and therefore lead to one of our principal conclusions, that the region producing the 86 GHz masers has a high kinetic temperature (§ 4.4).

The pumping network consists of various cycles connecting the upper and lower maser energy levels. The importance of any particular cycle depends on the populations of the levels involved. The population distribution within the torsional ground state is determined by an interplay of radiative and collisional processes. Collisional processes are negligible for transitions between different torsional states, so the populations of torsionally excited states are governed by the radiative transitions connecting them with the torsional ground state. Due to the selection rules for radiative transitions, the population distribution within each torsionally excited state roughly mirrors that within the torsional ground state.

Representatives of the strongest pumping cycles for the 107.0, 81.0, and 86.6 GHz transitions under the conditions of model A from Table 4 are shown in Figure 7. Heating cycles are shown with solid lines, cooling cycles are shown with dashed lines, and maser transitions are shown with dash-dotted lines. See Sobolev (1986, 1989) and Sobolev & Deguchi (1994b) for definitions. Any particular pumping cycle accounts for only a small fraction of the population transfer between maser levels because of the large number of possible cycles. For example, only 1% of the heating for the 86 GHz transition is accounted for by cycles with less than seven links. The energy levels in Figure 7 have been divided into two categories. Those energy levels through which the maser transition gains power, due to the dominance of heating cycles passing through that level over corresponding cooling cycles, are shown with solid lines. The levels through which the maser transition loses power are shown with dotted lines.

For the 107.0 GHz transition, almost all of the energy levels shown contribute to the heating process, which explains the strength of this maser. Collisional processes play a role in determining the populations of the various levels. But since most levels are involved in heating, the maser brightness should be relatively insensitive to kinetic temperature and density, as seen in Figure 5 for most of the parameter range. The strongest heating cycles involve levels of low J and K (Fig. 7), so there is a slow decline in brightness with increasing temperature or density, as the population is redistributed to generally higher values of J and K.

In contrast, only a limited number of levels provide power to the 81.0 GHz transition under the high-temperature, high-density conditions of model A (Fig. 7). All of these levels have $K \leq 2$ and $J \leq 10$. Therefore, this maser is predicted to be weak, except under conditions of low kinetic temperature and low density (Fig. 5) that allow significant populations in the low-K, low-J levels.

The 86 GHz transitions under the conditions of model A acquire strength through the bulk of the energy levels. Therefore, these masers are predicted to be moderately strong at high density and high temperature. The representative heating cycle shown in Figure 7 demonstrates that much of the 86 GHz transition's strength is acquired through levels with rather high values of J and K. This suggests the existence of a threshold in kinetic temperature needed to populate those levels, as is seen in Figure 5. The maser brightness is relatively insensitive to kinetic temperature once this threshold is exceeded.

The dependence of the pumping on the gas kinetic temperature can also be considered from a thermodynamic perspective. The radiation from hot dust provides the source of energy and at low-temperature collisions provide the sink. The gas temperature therefore affects the characteristic temperature of the sink. It is well known that the degree of inversion (i.e., pump efficiency) is generally proportional to the difference of inverse characteristic temperatures of the source and the sink (Strelnitskij 1984; Bolgova, Makarov, & Sobolev 1988). So making the temperatures of the source and sink closer decreases the maser intensities. Figure 5 demonstrates that most methanol maser transitions follow this tendency over the range 50 K $\lesssim T_{kin} \lesssim$ 175 K.

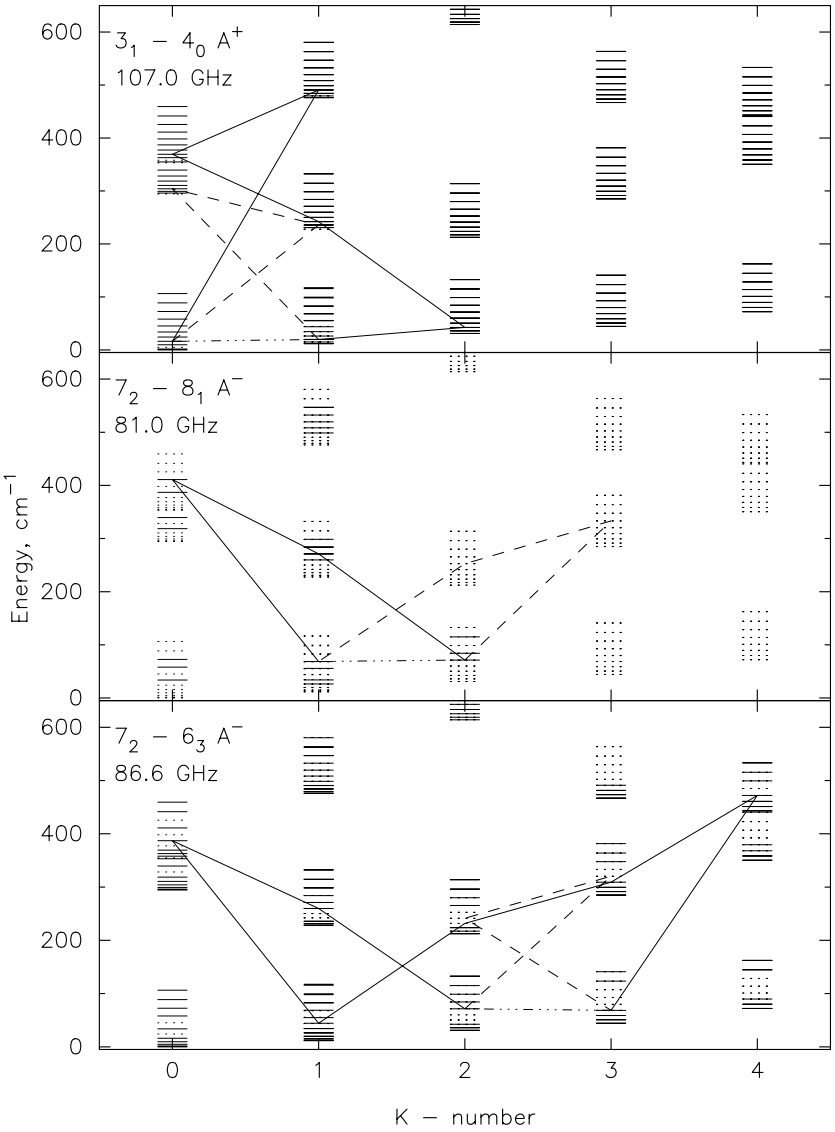

FIG. 7.—Pumping network for the 107.0 GHz 3_1–4_0 A^+, 86 GHz 7_2–6_3 $A^\pm$, and 81.0 GHz 7_2–8_1 A^- transitions, under the conditions of model A (Table 4). Energy levels up to $J = 11$ are shown for $v_t = 0$, 1, and 2 and $K = 0$, 1, 2, 3, and 4. Energy levels through which the maser gains power are shown with solid lines, and those through which the maser loses power are shown with dotted lines. For each maser the strongest heating cycle is shown with solid lines and the strongest cooling cycle with dashed lines. An individual cycle is responsible for only a small fraction of the maser power. The maser transitions themselves are shown with dash-dotted lines.

The variation in maser brightness with hydrogen density can be explained in terms of collisional quenching. At low density, collisions are infrequent, and all masers exhibit a plateau in brightness (Fig. 5). As the rate of collisions increases, the energy levels start to get thermalized, with the lower energy levels thermalized first. So the 81.0 GHz maser, which is pumped through levels of low J and K, begins to thermalize at densities of 10^5–10^6 cm^{-3}. The 86 and 107.0 GHz masers thermalize at higher density.

Thus, we can see that both high kinetic temperature and high density cause a decrease in the brightness of the 81.0 GHz maser relative to the 86 and 107.0 GHz masers. In fact, high values of both parameters are needed to fit our observational results, as described in § 4.4. We have provided a general explanation for this in terms of network analysis, but the complete pumping network is exceedingly complex. A more complete description of this network is beyond the scope of the current paper.

APPENDIX B

MODEL DEFICIENCIES

Our model has several deficiencies, major ones being (1) the simple LVG approximation for radiative transfer, (2) inadequacies in the dust opacity model, and (3) inadequacies in the collisional model. The first of these comes from the fact that the LVG approximation is a local treatment of radiative transfer, which does not take into account variations of the source

function within the object. Such variations have already been introduced in our discussion of "other" maser regions in § 4.4. The molecular region around W3(OH) is probably far from uniform in density and temperature. In this work we have identified one region, responsible for the 107 and 86 GHz masers. Other maser lines, particularly those at lower frequencies, are rather easily excited under different physical conditions, for example, in the low-density, radiatively dominated regime. In addition, certain details of the interaction of partly coherent radiation with the medium are not taken into account. Although the current study is restricted to regimes in which the masers are not highly saturated, such effects can be important for models of saturated masers. A model attempting to simultaneously fit all of the observed methanol masers would have to take into account source structure and possible saturation effects.

In our model we have also assumed a simple λ^{-2} dust opacity law. Since dust emission provides the radiative pumping for the masers, changes in dust spectra would alter the rates at which different transitions are pumped. Calculations to date that model the effects of grains of different composition and size (Ostrovskii & Sobolev 2000) in some cases predict significant changes in brightness temperature ratios. However, our basic conclusion that the 107 and 86 GHz masers are produced in a high-density, high-temperature region seems to be robust under such changes.

The collisional excitation rates adopted may also be incorrect. In general, we use the collision model of Peng & Whiteoak (1993), based on propensity rules derived from double-resonance experiments on *E*-species methanol. We have also tried some models with the collisional propensity rules suggested by Johnston et al. (1992) and with a nonselective collision model as in Sobolev et al. (1997b). The nonselective collision model does produce some significant changes but still obtains the best fit in the high-density, high-temperature regime. The collision model of Peng & Whiteoak (1993) is undoubtedly inadequate, but it seems to be a reasonable choice until accurate rates are calculated.

REFERENCES

Anderson, T., Herbst, E., & De Lucia, F. C. 1992, ApJS, 82, 405
Bachiller, R., Liechti, S., Walmsley, C. M., & Colomer, F. 1995, A&A, 295, L51
Barrett, A. H., Schwartz, P. R., & Waters, J. W. 1971, ApJ, 168, L101
Batrla, W., Matthews, H. E., Menten, K. M., & Walmsley, C. M. 1987, Nature, 326, 49
Baudry, A., Diamond, P. J., Booth, R. S., Graham, D., & Walmsley, C. M. 1988, A&A, 201, 105
Baudry, A., & Menten, K. M. 1995, A&A, 298, 905
Baudry, A., Menten, K. M., Walmsley, C. M., & Wilson, T. M. 1993, A&A, 271, 552
Baudry, A., Walmsley, C. M., Winnberg, A., & Wilson, T. L. 1981, A&A, 102, 287
Bloemhof, E. E., Reid, M. J., & Moran, J. M. 1992, ApJ, 397, 500
Bolgova, G. T., Makarov, S. V., & Sobolev, A. M. 1988, Astrophysics, 28, 239
Breckenridge, S. M., & Kukolich, S. G. 1995, ApJ, 438, 504
Caselli, P., Hasegawa, T. I., & Herbst, E. 1993, ApJ, 408, 548
Cesaroni, R., & Walmsley, C. M. 1991, A&A, 241, 537
Cragg, D. M., Johns, K. P., Godfrey, P. D., & Brown, R. D. 1992, MNRAS, 259, 203
Cragg, D. M., Sobolev, A. M., Ellingsen, S. P., Caswell, J. L., Godfrey, P. D., Salii, S. V., & Dodson, R. G. 2001, MNRAS, 323, 939
Dreher, J. W., & Welch, W. J. 1981, ApJ, 245, 857
Friberg, P., Madden, S. C., Hjalmarson, Å., & Irvine, W. M. 1988, A&A, 195, 281
Garcia-Barreto, J. A., Burke, B. F., Reid, M. J., Moran, J. M., Haschick, A. D., & Schilizzi, R. T. 1988, ApJ, 326, 954
Guilloteau, S., Baudry, A., & Walmsley, C. M. 1985, A&A, 153, 179
Guilloteau, S., Stier, M. T., & Downes, D. 1983, A&A, 126, 10
Hartquist, T. W., Menten, K. M., Lepp, S., & Dalgarno, A. 1995, MNRAS, 272, 184
Haschick, A. D., Baan, W. A., & Menten, K. M. 1989, ApJ, 346, 330
Hildebrand, R. H. 1983, QJRAS, 24, 267
Humphreys, R. M. 1978, ApJS, 38, 309
Johnston, K. J., Gaume, R., Stolovy, S., Wilson, T. L., Walmsley, C. M., & Menten, K. M. 1992, ApJ, 385, 232
Kawamura, J. H., & Masson, C. R. 1998, ApJ, 509, 270
Keto, E. R., Welch, W. J., Reid, M. J., & Ho, P. T. P. 1995, ApJ, 444, 765
Liechti, S., & Wilson, T. L. 1996, A&A, 314, 615
Mekhtiev, M. A., Godfrey, P. D., & Hougen, J. T. 1999, J. Mol. Spectrosc., 194, 171
Menten, K. M. 1991a, in ASP Conf. Ser. 16, Atoms, Ions, and Molecules: New Results in Spectral Line Astrophysics, ed. A. D. Haschick & P. T. P. Ho (San Francisco: ASP), 119
———. 1991b, ApJ, 380, L75
Menten, K. M., Johnston, K. J., Wadiak, E. J., Walmsley, C. M., & Wilson, T. L. 1988a, ApJ, 331, L41
Menten, K. M., Johnston, K. J., Wilson, T. L., Walmsley, C. M., Mauersberger, R., & Henkel, C. 1985, ApJ, 293, L83
Menten, K. M., Reid, M. J., Moran, J. M., Wilson, T. L., Johnston, K. J., & Batrla, W. 1988b, ApJ, 333, L83
Menten, K. M., Reid, M. J., Pratap, P., Moran, J. M., & Wilson, T. L. 1992, ApJ, 401, L39
Menten, K. M., Walmsley, C. M., Henkel, C., & Wilson, T. L. 1986, A&A, 157, 318
Menten, K. M., Walmsley, C. M., Henkel, C., & Wilson, T. L. 1988c, A&A, 198, 253
Moscadelli, L., Menten, K. M., Walmsley, C. M., & Reid, M. J. 1999, ApJ, 519, 244
Ostrovskii, A. B., & Sobolev, A. M. 2000, JENAM-2000: Joint European and National Astronomy Meeting (Moscow: GEOS), 172
Peng, R. S., & Whiteoak, J. B. 1993, MNRAS, 260, 529
Reid, M. J., Argon, A. L., Masson, C. R., Menten, K. M., & Moran, J. M. 1995, ApJ, 443, 238
Reid, M. J., Haschick, A. D., Burke, B. F., Moran, J. M., Johnston, K. J., & Swenson, G. W. 1980, ApJ, 239, 89
Slysh, V. I., Kalenskii, S. V., & Val'tts, I. E. 1992, ApJ, 397, L43
———. 1995, ApJ, 442, 668
Slysh, V. I., Kalenskii, S. V., Val'tts, I. E., Golubev, V. V., & Mead, K. 1999a, ApJS, 123, 515
Slysh, V. I., Val'tts, I. E., Kalenskii, S. V., & Larionov, G. M. 1999b, Astron. Rep., 43, 657
Sobolev, A. M. 1986, Soviet Astron., 30, 399
———. 1989, Astron. Nachr., 310, 343
———. 1993, Astron. Lett., 19, 293
Sobolev, A. M., Cragg, D. M., & Godfrey, P. D. 1997a, A&A, 324, 211
———. 1997b, MNRAS, 288, L39
Sobolev, A. M., Cragg, D. M., Salii, S. V., Kalinina, N. D., & Ellingsen, S. P. 1999, The Physics and Chemistry of the Interstellar Medium, ed. V. Ossenkopf, J. Stutzki, & G. Winnewisser (Herdecke: GCA), 299
Sobolev, A. M., & Deguchi, S. 1994a, A&A, 291, 569
———. 1994b, ApJ, 433, 719
Strelnitskij, V. S. 1984, MNRAS, 207, 339
Tsunekawa, S., Ukai, T., Toyama, A., & Takagi, K. 1995, Microwave Frequencies of the CH_3OH Molecule in the Frequency Range from 7 to 200 GHz (report for Grant-in-Aid for Scientific Research on Priority Areas, Interstellar Matter, 1991-1994, of the Ministry of Education, Science, and Culture, Japan; Toyama: Toyama Univ.)
Turner, J. L., & Welch, W. J. 1984, ApJ, 287, L81
Val'tts, I. E., Dzura, A. M., Kalenskii, S. V., Slysh, V. I., Booth, R. S., & Winnberg, A. 1995, A&A, 294, 825
Val'tts, I. E., Ellingsen, S. P., Slysh, V. I., Kalenskii, S. V., Otrupcek, R., & Voronkov, M. A. 1999, MNRAS, 310, 1077
van Buren, D., Mac Low, M.-M., Wood, D. O. S., & Churchwell, E. 1990, ApJ, 353, 570
Wilner, D. J., Reid, M. J., & Menten, K. M. 1999, ApJ, 513, 775
Wilson, T. L., Hüttemeister, S., Dahmen, G., & Henkel, C. 1993, A&A, 268, 249
Wilson, T. L., Johnston, K. J., & Mauersberger, R. 1991, A&A, 251, 220
Wilson, T. L., Walmsley, C. M., Menten, K. M., & Hermsen, W. 1985, A&A, 147, L19
Wilson, T. L., Walmsley, C. M., Snyder, L. E., & Jewell, P. R. 1984, A&A, 134, L7
Wink, J. E., Duvert, G., Guilloteau, S., Gusten, R., Walmsley, C. M., & Wilson, T. L. 1994, A&A, 281, 505
Wyrowski, F., Schilke, P., Walmsley, C. M., & Menten, K. M. 1999, ApJ, 514, L43
Xu, L.-H., & Lovas, F. J. 1997, J. Phys. Chem. Ref. Data, 26, 17